



## Crust and upper mantle structure of the Transantarctic Mountains and surrounding regions from receiver functions, surface waves, and gravity: Implications for uplift models

**Jesse F. Lawrence**

*Department of Earth and Planetary Sciences, Washington University, Campus Box 1169, 1 Brookings Drive, St. Louis, Missouri 63130, USA*

*Now at IGPP, Scripps Institution of Oceanography, 9500 Gilman Drive, IGPP 0225, La Jolla, California 92093, USA (jlawrence@ucsd.edu)*

**Douglas A. Wiens**

*Department of Earth and Planetary Sciences, Washington University, Campus Box 1169, 1 Brookings Drive, St. Louis, Missouri 63130, USA*

**Andrew A. Nyblade and Sridhar Anandakrishnan**

*Department of Geosciences, Pennsylvania State University, 447 Deike Building, University Park, Pennsylvania 16802, USA*

**Patrick J. Shore**

*Department of Earth and Planetary Sciences, Washington University, Campus Box 1169, 1 Brookings Drive, St. Louis, Missouri 63130, USA*

**Donald Voigt**

*Department of Geosciences, Pennsylvania State University, 447 Deike Building, University Park, Pennsylvania 16802, USA*

[1] This study uses seismic receiver functions, surface wave phase velocities, and airborne gravity measurements to investigate the structure of the Transantarctic Mountains (TAM) and adjacent regions of the Ross Sea (RS) and East Antarctica (EA). Forty-one broadband seismometers deployed during the Transantarctic Mountain Seismic Experiment provide new insight into the differences between the TAM, RS, and EA crust and mantle. Combined receiver function and phase velocity inversion with niching genetic algorithms produces accurate crustal and upper mantle seismic velocity models. The crustal thickness increases from  $20 \pm 2$  km in the RS to a maximum of  $40 \pm 2$  km beneath the crest of the TAM at  $110 \pm 10$  km inland. Farther inland, the crust of EA is uniformly  $35 \pm 3$  km thick over a lateral distance greater than 1300 km. Upper mantle shear wave velocities vary from  $4.5 \text{ km s}^{-1}$  beneath EA to  $4.2 \text{ km s}^{-1}$  beneath RS, with a transition between the two at  $100 \pm 50$  km inland near the crest of the TAM. The  $\sim 5$  km thick crustal root beneath the TAM has an insufficient buoyant load to explain the entire TAM uplift, suggesting some portion of the uplift may result from flexure associated with a buoyant thermal load in the mantle beneath the edge of the TAM lithosphere.



**Components:** 12,550 words, 13 figures, 3 tables, 1 dataset.

**Keywords:** Transantarctic Mountains; receiver functions; crustal thickness; phase velocity; flexure; thermal anomaly.

**Index Terms:** 7203 Seismology: Body waves; 7205 Seismology: Continental crust (1219); 7218 Seismology: Lithosphere (1236).

**Received** 22 February 2006; **Revised** 15 May 2006; **Accepted** 29 August 2006; **Published** 18 October 2006.

Lawrence, J. F., D. A. Wiens, A. A. Nyblade, S. Anandakrishnan, P. J. Shore, and D. Voigt (2006), Crust and upper mantle structure of the Transantarctic Mountains and surrounding regions from receiver functions, surface waves, and gravity: Implications for uplift models, *Geochem. Geophys. Geosyst.*, 7, Q10011, doi:10.1029/2006GC001282.

## 1. Introduction

[2] The Transantarctic Mountains (TAM) are a spectacular 3500 km long mountain range which marks the boundary between cratonic East Antarctica, and adjacent regions of Mesozoic and Cenozoic assembly (West Antarctica) [Dalziel, 1992]. The TAM represent the largest noncollisional mountain range in the world [ten Brink et al., 1997], and there has been considerable debate about the nature of the uplift mechanism.

[3] A number of models have been proposed to explain the uplift of the Transantarctic Mountains, including delayed phase changes (eclogite to basalt or quartz-eclogite to granulite) [Smith and Drewry, 1984], simple shear extension [Fitzgerald et al., 1986], various kinds of flexure models [Stern and ten Brink, 1989; Bott and Stern, 1992; ten Brink et al., 1993; ten Brink and Stern, 1992], plastic [Chery et al., 1992] and elastic [van der Beek et al., 1994] necking models, transform-flank uplift [ten Brink et al., 1997], and collapse of a high plateau, with thick crust providing buoyancy [Studinger et al., 2004]. A central question in the debate about the origin of the TAM is whether the uplift is provided by thermal buoyancy due to perturbed upper mantle temperatures [e.g., ten Brink et al., 1997], or by thickened crust [Studinger et al., 2004]. The principal assumption made in many of the tectonic models is that thermally perturbed mantle lithosphere extends underneath the TAM, providing buoyancy.

[4] Much of the uncertainty in the origin of the TAM results from a lack of constraint on crustal and upper mantle structure. In particular, the notions that the TAM crust is thicker than the surrounding crust of East Antarctica, or that thermally perturbed lithosphere extends beneath the

TAM, have not been fully tested seismologically. This study uses a new set of broadband seismic and aerogeophysical data from the Transantarctic Mountain Seismic Experiment (TAMSEIS) to model the crustal and upper mantle structures of East Antarctica, the West Antarctica Rift System, and the Transantarctic Mountains between the Ross Sea and the Vostok Subglacial Highlands (Figure 1). The Transantarctic Mountain Seismic Experiment consisted of 41 broadband seismometers deployed between the Ross Sea and the Vostok Subglacial Highlands from November, 2000 and December, 2003. Accompanying aerogeophysical data were collected by the US National Science Foundation's Support Office for Aerogeophysical Research (SOAR) in the 1999/2000 [Blankenship et al., 2001; Holt, 2001; Richter et al., 2001; Studinger et al., 2004] and 2000/2001 austral summers.

[5] Phase velocities and receiver functions from TAMSEIS are uniquely appropriate geophysical tools for differentiating between geodynamic models of the TAM. Teleseismic *P*-wave receiver functions and Rayleigh wave phase velocities are inherently complementary. Receiver functions can be used to locate seismic velocity discontinuities and gradients but provide poor constraints on the actual velocities and suffer trade-off between discontinuity depth and velocity structure, whereas surface waves provide better constraints on the velocities, but provide little information about discontinuity depth. The combined inversion of receiver functions and localized phase velocity curves [Julia et al., 2000; Chang et al., 2004; Lawrence and Wiens, 2004] provides excellent estimates of crustal thickness and seismic velocity underlying each station. In this study we use the Rayleigh wave phase velocity tomography results from Lawrence et al. [2006a] to help constrain the

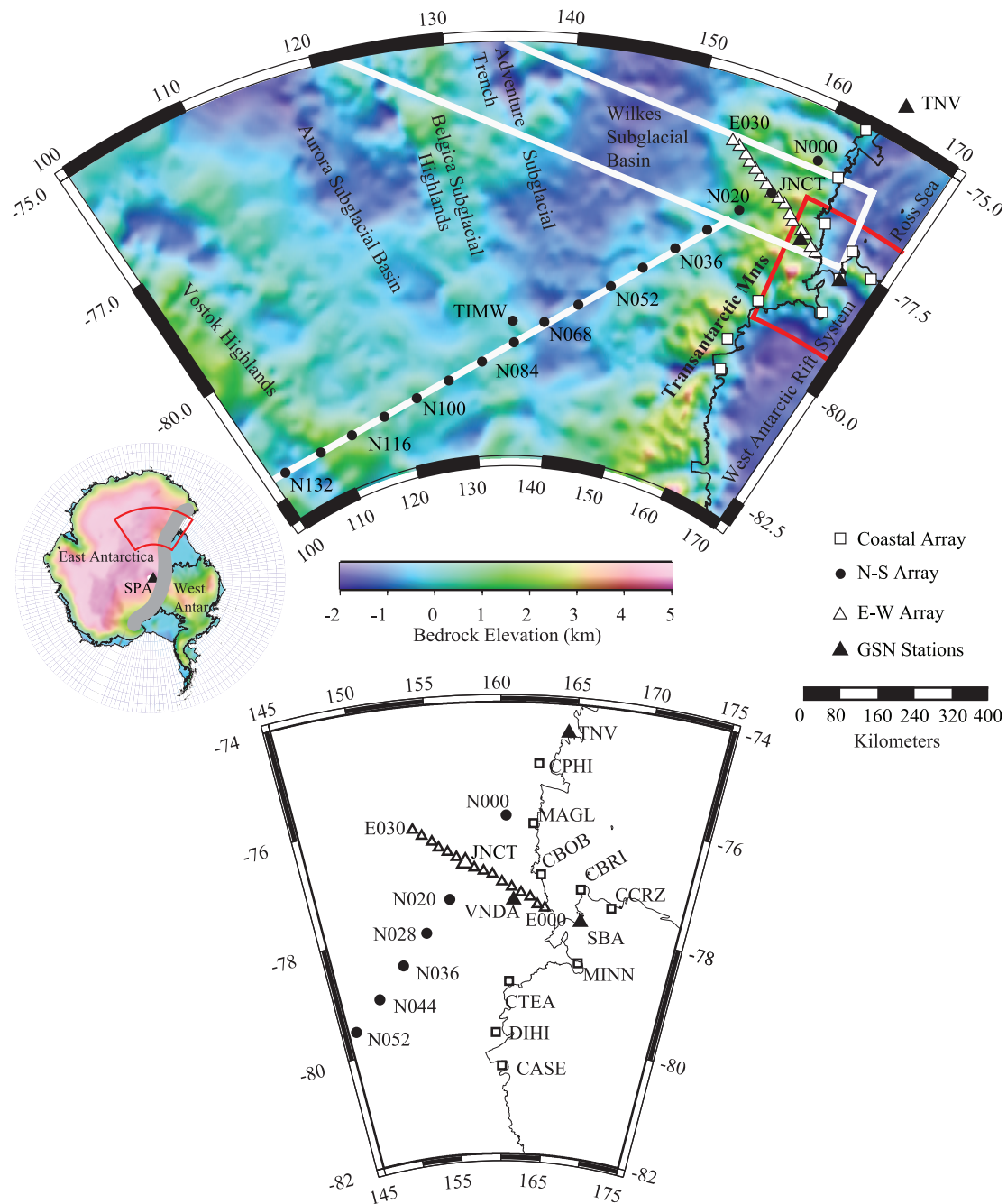


**Figure 1.** A map of the seismic stations used in this study overlain on shaded relief bedrock topography from BEDMAP [Lythe *et al.*, 2001]. The triangles, circles, and squares show seismometer locations. The white box and lines show airborne geophysics surveys flown between 1999 and 2001 [Blankenship *et al.*, 2001; Holt, 2001]. The red lines outline the region where other geophysical data were supplemented (ADGRAV, <http://www.marine-geo.org/antarctic/gravity/>, 2004).

receiver function inversions for the structure beneath each TAMSEIS station.

[6] In the following sections we first review the regional tectonic features and previous geophysical

work, and describe the data set and methods used in the seismic analyses. The results and interpretation of the various seismic analyses are then presented. The seismic results are combined with gravity and topography data to evaluate various



geophysical models for the uplift of the Transantarctic Mountains.

## 2. Regional Setting and Previous Work

### 2.1. Regional Tectonics and Geological History

[7] The study area is divided into three primary tectonic regions; East Antarctica (EA); the Ross Sea (RS); and the Transantarctic Mountains (TAM) (Figure 1). East Antarctica is a topographically high [Cogley, 1984], 35–45 km thick crustal block [Bentley, 1991], associated with a Precambrian craton that held a central position in the Paleozoic supercontinent, Gondwana [Tingey, 1991]. The RS comprises a portion of West Antarctica (WA), which is an amalgamation of low-lying, 20–35 km thick, younger crustal blocks [Dalziel and Elliot, 1982; Janowski and Drewry, 1981]. The Transantarctic Mountains are approximately 3500 km long and 200 km wide, dividing EA from WA with peaks that rise over 4 km above sea level. Crustal thickness estimates under the TAM vary between 20 and 45 km [Bannister et al., 2003; Buseti et al., 1999; Cooper et al., 1997; Kanao et al., 2002; ten Brink et al., 1993, 1997].

[8] The TAM differ from most mountain ranges of similar size and lateral extent because they lack evidence of a compressional origin. The TAM crust uplifted  $\sim 6$  km in an asymmetric tilt block formation and underwent denudation from the Cretaceous to the Cenozoic [Fitzgerald, 1992, 1995; Studinger et al., 2004]. The cause of the rock uplift and denudation is the subject of continuing debate. The interpretation of the modern geology is complicated by prior tectonic activity. Subduction-related mountain building, rifting, denudation, subsidence and formation of thick sedimentary layers, and volcanic intrusion and extrusion altered the crust and lithosphere of the TAM prior to the formation of the current mountains (see Fitzgerald [2002] for a general review). The Cenozoic-Cretaceous asymmetric uplift and subsequent erosion exposed basement rock and older sediments along the coastward side of the TAM, leaving younger sediments only on the inland side.

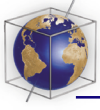
[9] In the Ross Sea, the TAM are bordered on the eastern side by part of the West Antarctic Rift System (WARS), a broad region of thinned continental crust associated with Cretaceous and episodic Cenozoic extension [Behrendt, 1999; Behrendt et al., 1991a, 1991b]. The WARS has

high heat flow ( $83\text{--}126\text{ mWm}^{-2}$ ) [Berg et al., 1989; Blackman et al., 1987] and thick (5–14 km) sedimentary basins with recent faulting [Cande and Leslie, 1986; Cooper et al., 1987; Hamilton et al., 2001]. The Ross Archipelago [LeMasurier and Thomson, 1990] is currently active with alkaline volcanism at Mt. Erebus and Mt. Melbourne. The crust in the WARS is currently  $\sim 19 \pm 2$  kilometers thick [Cooper et al., 1997; Trehu, 1989]. Spreading/extension within the western Ross Sea [Cande et al., 2000] has coincided with enormous sediment infilling from the Oligocene to present [Hamilton et al., 2001; Cape Roberts Science Team, 2000].

[10] The Wilkes Subglacial Basin (WSB) borders the TAM on the inland side (Figure 1). The WSB is a long wavelength negative topographic feature that may be filled with several kilometers of sediment [Drewry, 1976]. There are two different models for the formation of WSB. Deflection by over a kilometer may have resulted as a flexural response to Transantarctic Mountain uplift [Stern and ten Brink, 1989; ten Brink et al., 1997]. Alternatively, the basin may have formed as a result of rifting [Drewry, 1976; Ferraccioli et al., 2001]. Studinger et al. [2004] suggest that the WSB simply represents a low region of thinner crust between the TAM and the Belgica Subglacial Highlands further inland (Figure 1). The Aurora Subglacial Basin is a long wavelength, negative topographic ( $\sim 1$  km) feature between the Belgica Subglacial Highlands and the Vostok Subglacial Highlands. The Vostok Subglacial Highlands may represent a tectonic boundary between the thinner ( $\sim 35$  km) crust to the east of  $105^\circ$  and the thicker crust to the west of  $100^\circ$  underlying the Gamburtsev Subglacial Mountains [Studinger et al., 2003].

### 2.2. Previous Seismological Studies

[11] Continental- and global-scale surface wave velocity studies [Danesi and Morelli, 2001; Ritzwoller et al., 2001; Sieminski et al., 2003; Morelli and Danesi, 2004] demonstrate that the TAM lay on the boundary between seismically fast East Antarctic mantle and seismically slow West Antarctic mantle. These studies find sharp lateral velocity gradients that may imply a sharp boundary between East and West Antarctica running the length of the TAM. However, due to the relative lack of seismicity and seismometers in the Antarctic interior, the resolution of these seismic models is limited to several hundreds of kilometers. Phase velocity maps inverted from Rayleigh waves measured at 41 TAMSEIS and 5



Global Seismic Network (GSN) stations establish that the transition occurs between 50 and 150 km inland from the coast beneath the TAM [Lawrence *et al.*, 2006a]. Body wave tomography results [Watson *et al.*, 2006] and attenuation measurements [Lawrence *et al.*, 2006b] from TAMSEIS data confirm that a major transition from fast seismic velocities and low attenuation in EA to low seismic velocities and high attenuation in RS occurs between 50 and 150 km from the coast.

[12] Several small-scale studies examined the structure of the Transantarctic Mountains with surface waves [Bannister *et al.*, 2000], and receiver functions [Bannister *et al.*, 2003; Kanao *et al.*, 2002]. The studies of Bannister *et al.* [2000] and Kanao *et al.* [2002] used seismograms from three Global Seismic Network stations to respectively demonstrate that the Transantarctic Mountains possessed faster mantle shear wave velocities and thicker crust than the West Antarctic Rift System. Bannister *et al.* [2003] used receiver functions from VNSA, SBA, and a 10-seismometer experiment deployed during the 1999 austral summer to demonstrate that the crust decreased from  $38 \pm 2$  km at  $\sim 85$  km inland from the coast to  $31 \pm 2$  km at  $\sim 10$  km from coast. Bannister *et al.* [2003] also demonstrated that the coastal and Ross Island crust is  $\sim 20$  km thick. Short period ( $< 25$  second) Rayleigh wave phase velocity maps show a clear transition from fast to slow velocities across the TAM that are interpreted as a transition from thin ( $\sim 20$  km) to thick crust ( $> 30$  km), with the transition extending along the TAM front for  $\sim 500$  km [Lawrence *et al.*, 2006a]. Results from active source seismic experiments [e.g., Cooper *et al.*, 1997] are consistent with these results.

[13] Lawrence *et al.* [2006b] found excellent agreement between phase velocity variation and attenuation variation, which suggests a significant ( $\sim 300$  K) increase in mantle temperature from EA to WA. The  $\sim 300$  K temperature increase is likely accompanied by a  $\sim 1\%$  density decrease from EA to WA.

### 2.3. Geophysical Models for Transantarctic Mountains Uplift

[14] Geophysical studies have examined the Transantarctic Mountains using topography, gravity, ice thickness, and magnetics to model several possible mechanisms for uplift. Stern and ten Brink [1989] suggest that the topographic geometry of the TAM and WSB represents an asymmetric rift flank associated with the Cenozoic extension of the

WARs. The possible mechanisms for the uplift include thermal buoyancy due to conductive or advective heating from the hotter West Antarctic lithosphere [Stern and ten Brink, 1989; ten Brink and Stern, 1992], simple shear extension [Fitzgerald *et al.*, 1986], isostatic rebound following normal faulting [Bott and Stern, 1992], plastic necking [Chery *et al.*, 1992], elastic necking [van der Beek *et al.*, 1994], and rebound response to erosion [Stern and ten Brink, 1989]. ten Brink *et al.* [1997] fit gravity and bedrock topography data from the EAST93 geophysical traverse with a broken elastic plate model having elastic thickness  $T_e = 85 \pm 15$  km, and crustal thickness of 40 km. Studinger *et al.* [2004] assert that an Airy isostatic model of the Transantarctic Mountains with crustal thickness ranging from 30 to 40 km provides a better fit to airborne gravity and ice-penetrating radar measurements of bedrock topography than a purely elastic model without a mountain root.

### 3. Seismic Data

[15] This study employs three-component, broadband seismic data recorded at 44 seismic stations (41 TAMSEIS stations and 3 GSN stations) in Antarctica between November 2000 and December 2003. Three subarrays make up the TAMSEIS network (Figure 1, Table 1). The first array has 17-stations aligned roughly E-W with 20-km interstation spacing. This subarray crosses 300 km from the coast over the Transantarctic Mountains onto the East Antarctic Plateau. A second, 17-stations subarray extends southwest from Terra Nova (TNV), with  $\sim 80$  km interstation spacing. This subarray spans 1400 km into the Antarctic interior, traversing from the coast, over the TAM, and through the Wilkes Subglacial Basin, the Belgica Subglacial Highlands, the Aurora Subglacial Basin, and into the Vostok Subglacial Highlands. The third subarray consists of 9-stations at  $\sim 80$  km station spacing along the coast and on Ross Island.

[16] For receiver functions we analyze records of earthquakes with magnitude greater than 6.0  $m_b$  between  $30^\circ$  and  $90^\circ$  from the array (Figure 2) to ensure a high signal-to-noise ratio and a nearly vertical incident  $P$  wave. The data, originally sampled at 20 or 40 samples per second, are resampled at 20 samples per second to ensure identical treatment of all signals. Each waveform is visually inspected to ensure the presence of a high-quality  $P$  wave. Trends are removed from the data to reduce instrument drift and minimize the



**Table 1.** Seismic Stations

Station	Latitude	Longitude
<i>TAMSEIS Coastal Array</i>		
CPhi	-75.0745	162.6484
MAGL	-76.1381	162.4083
CBOB	-77.0342	163.1707
CBRI	-77.2516	166.4266
CCRI	-77.5166	169.0947
MINN	-78.5504	166.8800
CTEA	-78.9439	160.7643
DIHI	-79.8491	159.4800
CASE	-80.4481	160.1262
<i>TAMSEIS E-W Array</i>		
E000	-77.6262	163.6175
E002	-77.575	163.0078
E004	-77.4133	162.0661
E006	-77.3703	161.6256
E008	-77.2817	160.5033
E010	-77.1853	160.0098
E012	-77.0461	159.3247
E014	-76.9898	158.6217
E018	-76.8234	157.2237
E020	-76.7295	156.5472
E022	-76.628	155.9025
E024	-76.5346	155.2500
E026	-76.4248	154.7582
E028	-76.3075	154.0384
E030	-76.251	153.3793
<i>TAMSEIS N-S Array</i>		
N000	-76.0087	160.3784
JNCT	-76.9288	157.9012
N020	-77.4678	155.8175
N028	-78.0296	153.6509
N036	-78.5508	151.2776
N044	-79.0692	148.6159
N052	-79.5441	145.7489
N060	-80.0000	142.5936
N068	-80.3911	138.9200
N076	-80.8061	135.4326
N084	-81.1601	131.4673
N092	-81.4621	126.9822
N100	-81.691	122.4672
N108	-81.8791	117.6036
N116	-82.0094	112.5698
N124	-82.0741	107.6413
N132	-82.0751	101.9539
<i>GSN Stations</i>		
TNV	-74.7000	164.1200
VNDA	-77.5139	161.8456
SBA	-77.8491	166.7573

artifacts caused by filtering. The horizontal components of the receiver function data are rotated into radial and tangential components prior to deconvolution. For the surface wave constraints we use phase velocities at each station from the tomographic inversion of Raleigh wave interstation

phase velocities from the same station deployment by Lawrence *et al.* [2006a].

[17] We obtained at least 13 receiver functions from all seismic stations. More than 20 receiver functions were calculated for 37 seismic stations. More than 22 seismic stations yielded more than 60 receiver functions. The geographic distribution of the source earthquakes is good, providing a variety of back azimuths for receiver function calculation (Figure 2). Most of the earthquakes we analyzed were located along southern Pacific subduction zones and in Southeast Asia. Only a few events ruptured around the Antarctic Plate Boundary. The Tonga-Kermadec and South American subduction zone earthquakes provide a good distribution of epicentral distances.

## 4. Analysis

### 4.1. Receiver Functions

[18] Receiver functions isolate the localized crustal and upper mantle response to a teleseismic *P* wave by effectively removing the source function and mantle response through deconvolution of the radial horizontal *P*-coda with the vertical *P*-coda [Ammon, 1991; Ammon *et al.*, 1990; Langston, 1979]. While there are multiple methods for calculating receiver functions from observed data [Langston, 1979; Park and Levin, 2000; Reading *et al.*, 2003], we choose the iterative deconvolution method of Ligorria and Ammon [1999] to minimize acausal energy. We calculate two receiver functions for every recorded earthquake described above with two separate low-pass Gaussian filters, having a gain of 10% at 0.3 Hz and 1 Hz (Gaussian filter widths,  $a = 0.625$  and  $a = 2.1$  (C. J. Ammon, An overview of receiver-function analysis, <http://eqseis.geosc.psu.edu/~cammon/HTML/RftnDocs/rftn01.html>, 2004)). Using two different low-pass filters ensures that the long- and short-period responses are taken into account. Some of the final stacked receiver functions are available as auxiliary material<sup>1</sup> (Figure S1). Where sufficient data are available, multiple receiver function stacks are produced using earthquakes from a variety of distances and azimuths. While stacks from different distances are compared to ensure the stability of each stack, only stacks with the dominant distance range (predominantly  $\sim 15^\circ$  bins centered between  $60^\circ$  and  $80^\circ$ ) are used in the following analysis.

<sup>1</sup>Auxiliary materials are available in the HTML. doi:10.1029/2006GC001282.

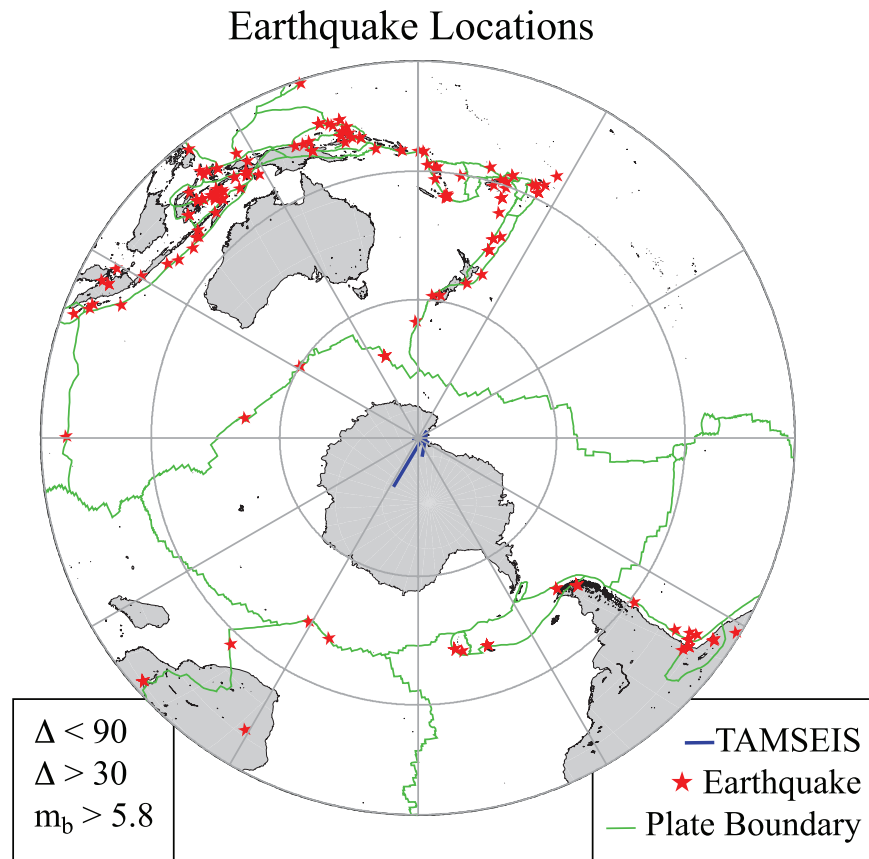


**Figure 2.** A map of earthquake locations (red stars) used for the receiver function analysis. The earthquakes provide a good distribution of back azimuth directions as well as event-to-station distances for the TAMSEIS array (blue). The plate boundaries are drawn in green. The gray lines delineate 30 degree increments in azimuth and distance from station E020.

The 60° to 80° distance range yields the best azimuthal coverage.

[19] The observed receiver functions demonstrate significant variation from east to west across the tightly spaced E-W array (Figure 3). In general the Ross Island and TAM receiver functions possess clearly visible *Ps* conversions relative to those observed at stations located on the East Antarctic Ice Plateau, and are similar to those observed by *Bannister et al.* [2003]. Perhaps the most notable signal for stations on the East Antarctic Plateau is the ice layer reverberation. For high-frequency receiver functions, the *Ps* conversion is clearly observed for rock stations, but becomes obscured by the ice reverberations for the ice stations. Longer period receiver functions show the Moho *Ps* conversion and multiples with less ambiguity, having less emphasis on the high-frequency ice reverberations.

[20] The receiver functions observed at Ross Island, show a strong reflector at 1–2 seconds suggesting a shallow low-velocity sediment layer [e.g., *Clitheroe et al.*, 2000; *Sheehan et al.*, 1995]. *Bannister et al.* [2003] modeled this pulse with simple 1-D models having three layers; sediment, crust, and mantle. The complex receiver function structure obscures, but does not remove, the Moho *Ps* conversion. This complex pulse is observed at all the Ross Island stations (SBA, CBRI, and CCRZ) with varying degrees, suggesting lateral variation in the sediment thickness.

[21] Through the Transantarctic Mountains the Moho *Ps* conversion becomes progressively more time delayed with distance from the coast. The Moho *Ps* amplitude for stations E008 and E006 are low, possibly indicating that the *Ps* conversion is stacking incoherently from a tilted interface. The *Ps* conversion arrives ~3 seconds after the initial pulse at the coast and ~5 seconds after the initial

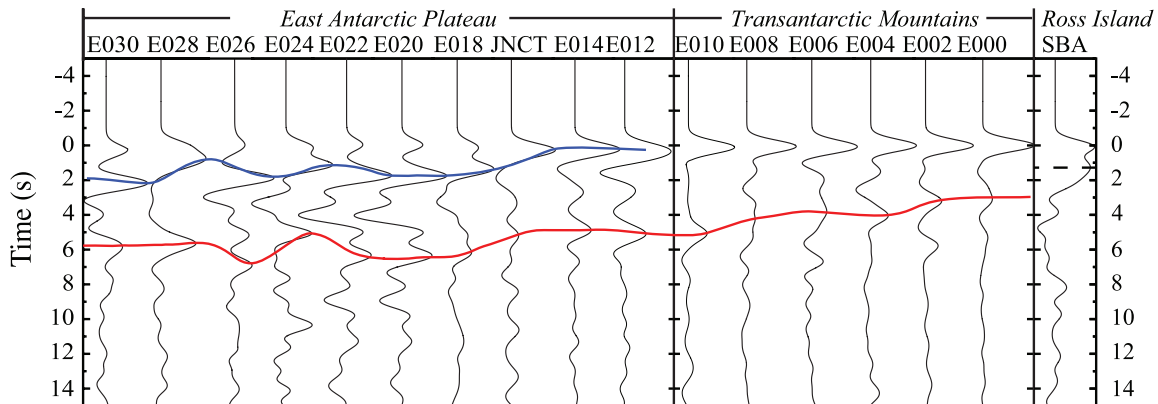


**Figure 3.** Receiver functions (filtered with Gaussian width  $\alpha = 2.1$ ) change rapidly along the E-W subarray. Large ice and sediment reverberations (blue line) are present between 1 and 3 seconds for stations located on the East Antarctic Ice Plateau and on Ross Island. The  $P_s$  phase (red line) changes significantly as a result of both depth and the presence or lack of a thick sediment or ice layer.

pulse at 100 km inland. Small conversions at 1–2 seconds may indicate additional shallow interfaces beneath the TAM from 20 to 80 km inland. There is no indication of strong azimuthal variation in the TAM receiver functions, which agrees with the findings of *Bannister et al.* [2003].

[22] The higher frequency receiver functions from seismic stations located on ice exhibit complex signals from 1 to 3 seconds of the initial  $P$  wave, similar to that observed at SBA. We are able to model these complex signals with simple 1-D models having ice, crust, and mantle layers. The ice thickness at each station, as determined from ice penetrating radar, provides an excellent match to the observed complex receiver functions (Figure 4). The ice  $P_s$  conversion clearly dominates the receiver function from 1–2 seconds. However, Moho depth is crucial for modeling the receiver function after  $\sim 2$  seconds. To demonstrate this, we calculated four receiver functions from models with the same ice layer velocity and thickness but different crustal thickness (18–45 km). While the receiver functions appear more similar to each other than non-ice-layer receiver functions with different Moho depths (Figure 5, left), the residuals from the average receiver function (Figure 5, right) indicate that they are quite different after  $\sim 2$  seconds. The moveout of the Moho  $P_s$  conversion (dashed line) as a result of layer thickness is clearly visible. The Moho  $P_s$  pulse for the ice-layer models has the same amplitude as the  $P_s$  pulse from non-ice-layer models. Consequently, providing ice thickness as an a priori constraint makes inversion possible for structure beneath the ice.

## 4.2. One-Dimensional Niching Genetic Algorithm Inversion

[23] We use the niching genetic algorithm (NGA) to invert receiver functions and phase velocities for 1-D velocity models [*Mahfoud, 1995; Koper et al., 1999; Lawrence and Wiens, 2004*]. The NGA efficiently searches the model space with an evolutionary paradigm by calculating receiver functions and phase velocities from multiple populations of 1-D velocity models, and removing models that have high L2 misfit (or cost) when compared to the observed data [*Lawrence and Wiens, 2004*]. Receiver functions are calculated

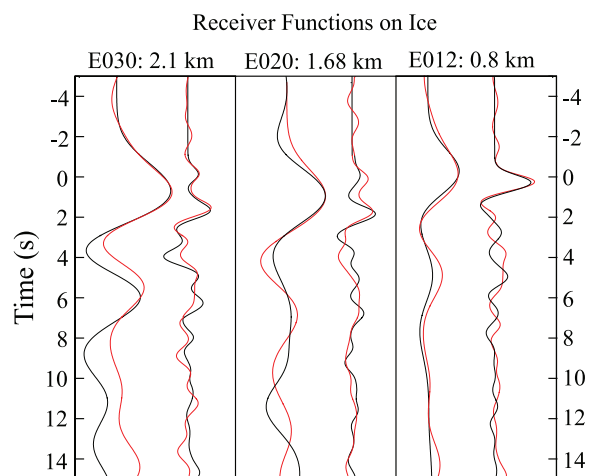


**Figure 4.** Receiver functions from stations on ice (black) and synthetic receiver functions (red) created with varying ice thickness from 3 layer models (Ice:  $V_S = 1.5 \text{ km s}^{-1}$  and  $V_p/V_S = 2.1$ ; Crust:  $V_S = 3.7 \text{ km s}^{-1}$  and 30 km thick; Mantle:  $V_S = 4.4 \text{ km s}^{-1}$ ; and rock Poisson's ratio: 0.25).

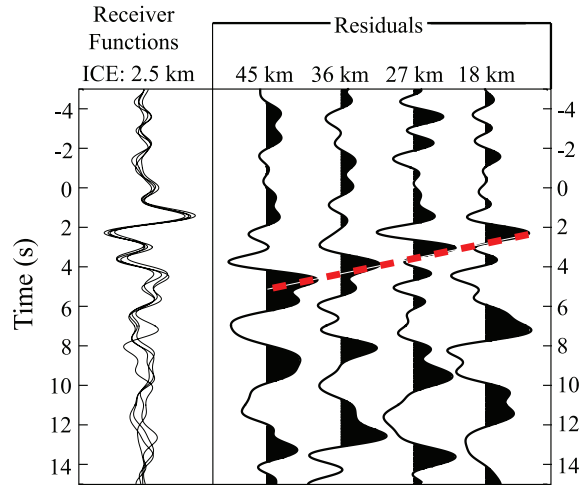
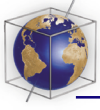


**Figure 5.** (left) Synthetic receiver functions and (right) deviations from the mean receiver functions created with varying crustal thickness from 3 layer models (Ice:  $V_S = 1.5 \text{ km s}^{-1}$ ,  $H = 2 \text{ km}$ ,  $V_P/V_S = 2.1$ ; Crust:  $V_S = 3.7 \text{ km s}^{-1}$  and  $35 \text{ km}$  thick; Mantle:  $V_S = 4.5 \text{ km s}^{-1}$ ; and rock Poisson's ratio: 0.25). The dashed line indicates the Moho  $P_S$  conversion.

from 1-D velocity models with the technique of *Randall* [1989] because it is computationally more efficient than other techniques. We invert for a 1-D velocity model for each of the 41 TAMSEIS stations and 3 GSN stations. The “isolated” phase velocity curve for each station is taken from the phase velocity maps of *Lawrence et al.* [2006a]. Models with low cost continue on to further generations where some of the model parameters are mutated and recombined with other models. In each subsequent generation the same comparisons and application of costs causes the NGA to remove unsuitable solutions and converge upon optimal solutions.

[24] The NGA is a compound genetic algorithm that makes several subpopulations compete against each other for the most optimal set of parameters. This is achieved by applying a similarity cost that effectively removes all models that are overly similar to higher-order subpopulations. Consequently, lower-order subpopulations are forced to search different volumes of the model space than the higher-order subpopulations. In this way, the NGA ensures that the entire model space is searched. For each set of data (2 receiver functions and the isolated phase velocity curve) the NGA runs for 250 generations, with 4 demes, and 20 models in each deme, adding up to a search of 20,000 models.

[25] The misfit cost is described in equation (1),

$$Cost = \left[ \sum_{i=1}^9 (V_{S_i} - 2V_{S_{i+1}} + V_{S_{i+2}}) \right]^{RW} \cdot \left[ \sum_{i=1}^N (R_{obs_i} - R_{syn_i})^2 / N \right]^{RF} \cdot \left[ \sum_{i=1}^M (D_{obs_i} - D_{syn_i})^2 / N \right], \quad (1)$$

where  $V_S$  is the shear velocity,  $RW$  is the roughness weighting,  $N$  is the number of observed,  $R_{obs}$ , and synthetic,  $R_{syn}$ , receiver function values,  $M$  is the number of observed  $D_{obs}$ , and synthetic,  $D_{syn}$ , Rayleigh phase velocity values, and  $RF$  is the receiver function misfit cost weighting. *Lawrence and Wiens* [2004] demonstrated that the inversion is relatively insensitive to a wide range of  $RW$  and  $RF$  values. Therefore  $RF$  and  $RW$  are set at 1.0 and 0.0625 respectively. Using both phase velocities and receiver functions requires much lower roughness weighting than do independent inversions of receiver functions or phase velocities.

[26] Each 1-D velocity model created by the NGA is parameterized with 8 layers and a half-space. Each layer is allowed to vary in both shear velocity ( $V_S$ ) and layer thickness ( $H$ ) as described in Table 2. For every three layers a single  $P$ -to- $S$  velocity ratio controls the  $P$  wave velocities. For stations located on the East Antarctic Plateau, a single low-velocity ice layer, with constant thickness determined by ice-penetrating radar [*Blankenship et al.*, 2001; *Holt*, 2001; *Richter et al.*, 2001; *Studingier et al.*, 2004], is exchanged for a rock layer. The known ice thickness frees a parameter for the independent determination of the  $P$  wave velocity ( $V_P$ ), so that it is not coupled with that of rock. The ice velocities

**Table 2.** One-Dimensional Model Parameterization

Layer	$H$ , km		$V_S$ , $\text{km s}^{-1}$		$V_P/V_S$	
	Min	Max	Min	Max	Min	Max
1	0.25	10	1.70	3.75	1.69	1.78
2	0.25	10	1.70	3.75		
3	0.25	10	2.20	4.20		
4	0.25	10	2.20	4.80	1.69	1.78
5	0.25	10	2.20	4.80		
6	0.25	10	3.00	4.80		
7	0.25	10	3.75	4.80	1.69	1.78
8	0.25	10	4.20	4.80		
9	Half-space		4.40	4.80		



are allowed to vary between 1.4 and 2.2 km s<sup>-1</sup> for  $V_S$  and between 2.8 and 4.4 km s<sup>-1</sup> for  $V_P$ . This large range in ice velocities accounts for variable fern layer thickness as a percent of the total ice layer thickness. Nevertheless, the resultant models only require shear ice velocities between 1.51 and 2.03 km s<sup>-1</sup>. In order to better model longer period phase velocities we add layers between 100 km and 400 km depth. These nonparameterized layers deeper than 100 km are created by applying a linear gradient shift to one of the three regional seismic velocity models (EA, TAM, WA) of *Lawrence et al.* [2006a] such that the velocities converge toward the “half-space” velocity of the parameterized model at shallow depths and equal the regional velocity model at 400 km.

[27] Potential bias can result from using slightly different receiver function calculations for the synthetics [*Randall, 1989*] and the observed data [*Ligorria and Ammon, 1999*]. The second method [*Ligorria and Ammon, 1999*] reduces acausal signal, which is most important with low signal-to-noise receiver functions. The first method [*Randall, 1989*] is only used to calculate synthetic receiver functions (without noise) so the bias is minimal. The method yields minimal bias and maximal accuracy in 1-D resolution tests with noise [*Lawrence and Wiens, 2004*].

[28] An optimal 1-D velocity model was determined for each of the 41 seismic stations using the NGA inversion [*Lawrence and Wiens, 2004*]. For stations with sufficient azimuthal coverage, separate models were obtained for each receiver function stack from a different azimuth. While only the dominant distance range having the best distribution of azimuths is presented here, the models obtained by inverting alternate subsets of the data are compared to those presented here to ensure reliability of results. Figure 6 depicts several examples of observed and synthetic receiver functions and phase velocity curves associated with the optimal models. For each seismic station we choose a single Moho depth associated with a large seismic velocity contrast between 17 and 45 km depth. For several seismic stations the best-fit models possess multiple velocity contrasts at very similar depths that result in more gradual Mohos. In such cases we choose the largest velocity contrast among the group. Additionally, the less optimal solutions with marginally higher NGA cost than the most-optimal model are used to help determine which interface is most appropriate. Such comparisons with less optimal models also

provide a rough estimate of the uncertainty in each Moho depth estimate. With just a few models, it is clear that the East Antarctic Moho is significantly deeper ( $35 \pm 3$  km) than that of West Antarctica ( $20 \pm 2$  km). Additionally, the shallow mantle velocity in East Antarctica ( $V_S \sim 4.5$  km s<sup>-1</sup>) is significantly faster than that of West Antarctica ( $V_S \sim 4.2$  km s<sup>-1</sup>).

### 4.3. Two-Dimensional Velocity Profiles

[29] By geographically compiling the 1-D models, we construct four 2-D vertical profiles through Antarctica. The locations of the profiles are shown in Figure 7. The first profile is a 120 km cross-section trending N-S through Ross Island to station MINN with 30–60 km lateral resolution. The second is a 640 km long profile along the coast with  $\sim 80$  km lateral resolution. The third profile follows the 300 km long E-W subarray across the Transantarctic Mountains into East Antarctica and has  $\sim 20$  km lateral resolution. The last profile follows the 1400 km N-S subarray through East Antarctica with  $\sim 80$  km lateral resolution.

## 5. Results

### 5.1. Crust and Upper Mantle Structure

[30] In the Ross Sea region (stations CBRI, CCRZ, SBA, and MINN) the crust is  $20 \pm 2$  km thick with low ( $4.2 \pm 0.1$  km s<sup>-1</sup>) upper mantle shear wave velocity (Figure 7a). Beneath Ross Island the Moho is observed as a gradient rather than a sharp boundary. There is a thick ( $>2$  km) low-velocity ( $<3$  km s<sup>-1</sup>) layer at the surface for all Ross Sea stations. A thick sediment/volcanic deposit layer is consistent with previous receiver function analysis [*Bannister et al., 2003*], active source seismic experiments [*Cooper et al., 1987; Hamilton et al., 2001*] and the Cape Roberts Drilling Project [*Cape Roberts Science Team, 2000*]. This sediment layer affects the timing and amplitude of the Moho  $P_s$  phase, which makes modeling the contrast and depth of the Moho less unique. However, given the large similarity between models of adjacent seismic stations and the complementary phase velocity constraints, we believe the structure is robust. Additionally, tradeoff analysis between less optimal models indicates that the Moho depths are relatively reliable [e.g., *Lawrence and Wiens, 2004*].

[31] At the coast (Figure 7b), the crust is relatively uniform in thickness varying from  $20 \pm 2$  km thick in the north to  $23 \pm 2$  km in the south. Upper

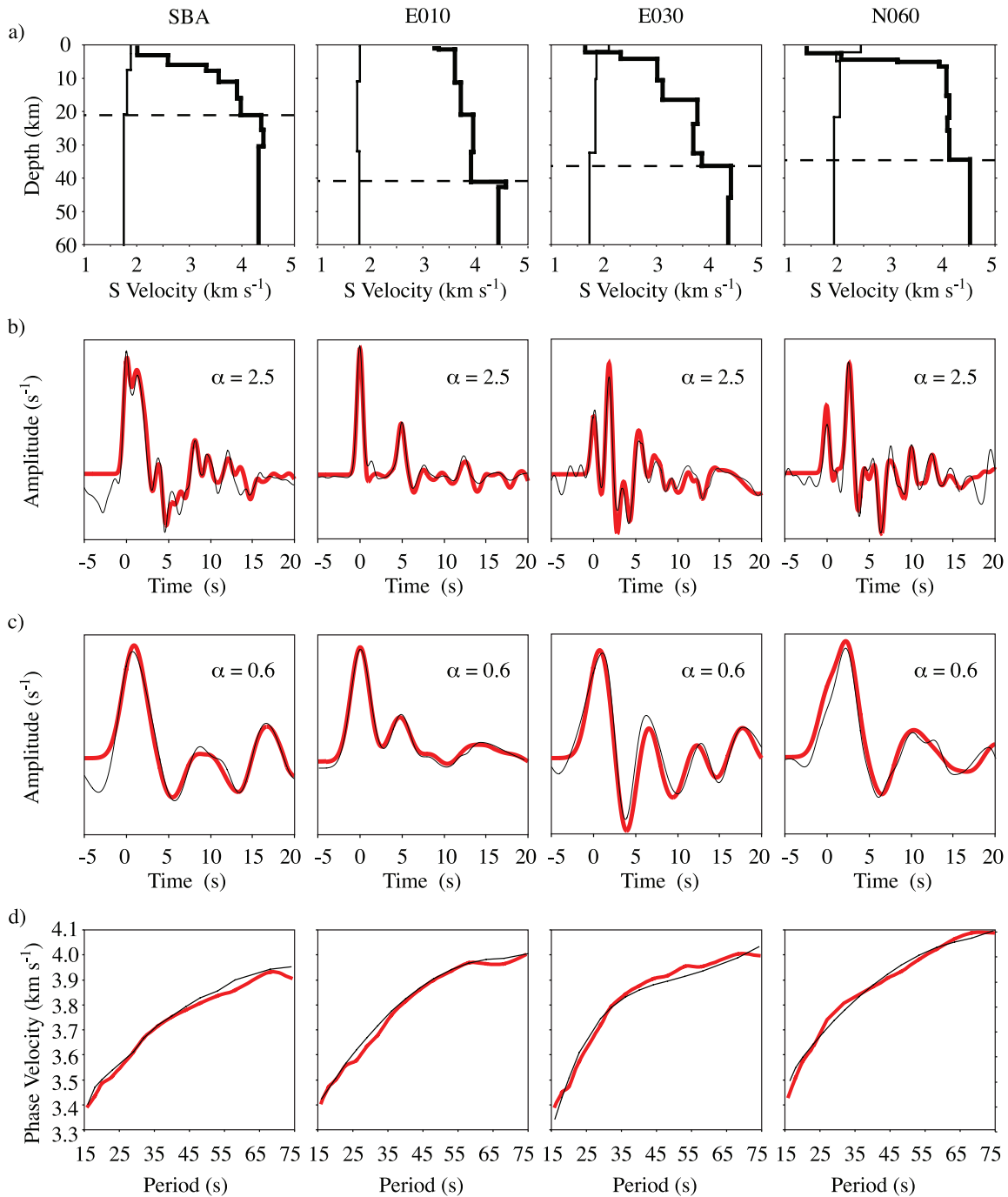


**Figure 6.** (a) The results from a 200-generation NGA inversion yield an excellent fit (black) to the data (red) for (b) high-frequency receiver functions, (c) low-frequency receiver functions, and (d) phase velocities for four stations (SBA, E010, E030, N060). The thick lines in Figure 6a indicate  $V_S$  velocity. The thin lines indicate the  $V_P/V_S$  ratio. The horizontal dashed lines in Figure 6a indicate the chosen Moho depth.

mantle shear wave velocity is  $\sim 4.2 \pm 0.2 \text{ km s}^{-1}$ . The velocity contrast at the Moho varies from diffuse with low contrast near E000 to sharp, having high contrast near CPHI. The mantle velocities are 2–3% lower at the center of the coastal

cross-section near E000. The highest mantle velocities along the mountain front (which are 2–3% lower than EA mantle velocities) occur at the southern edge of our study region. A low-velocity surface layer, probably representing sedimentary

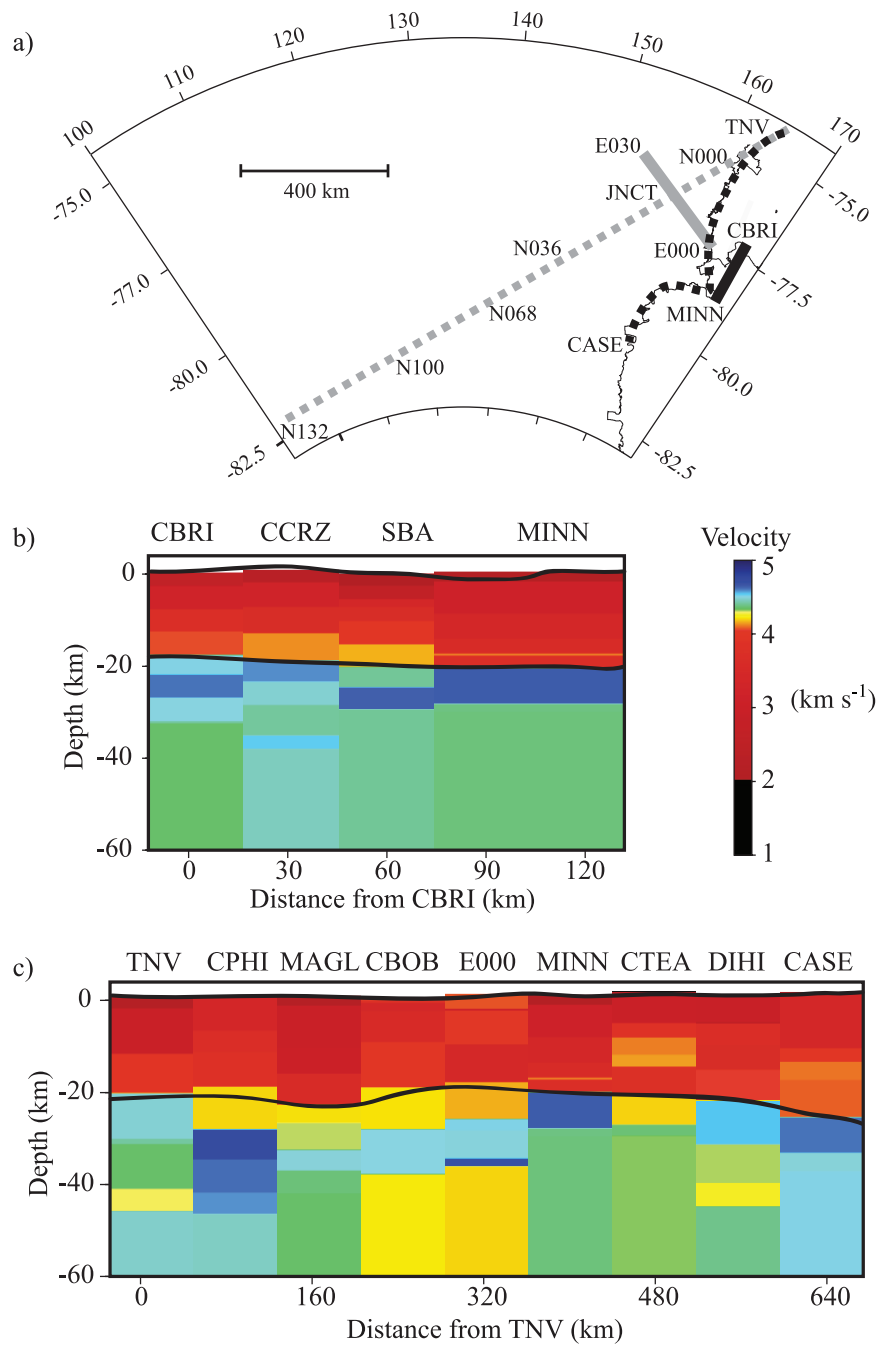
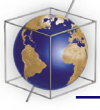


**Figure 7.** Two-dimensional profiles of shear velocity (Figure 7b) through Ross Island and (Figure 7c) along the coast were constructed from 1-D models like those seen in Figure 5. The surface topography and a smoothed Moho topography are drawn with black lines. The locations of these profiles are shown in Figure 7a. The solid black line is the Ross Island profile, the black dashed line is the coastal profile, the solid gray line is the E-W profile, and the dashed gray line is the N-S profile.

rocks, varies in thickness from 0 to 4 km. This layer may trade off with the depth and velocity contrast at the Moho by changing the timing and amplitude of the  $P_s$  conversion, especially for TNV, CBOB, and CASE. Nevertheless, the seismic

models for these stations are consistent with models from adjacent stations.

[32] Continuing westward along the E-W subarray (Figure 8), the models demonstrate a consistent

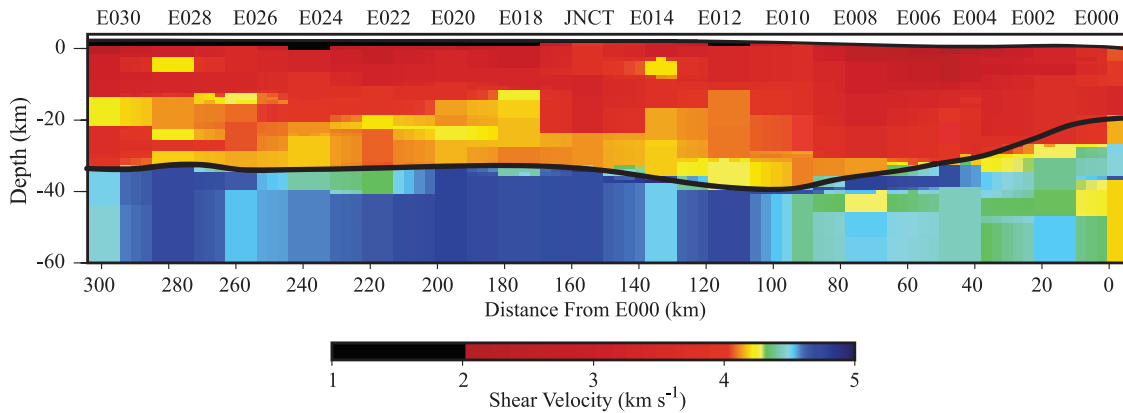


**Figure 8.** Two-dimensional profile of shear velocity for the E-W subarray across the TAM. The location of the profile is shown in Figure 6a.

trend with a deeper Moho to the west. The Moho reaches a maximum depth ( $40 \pm 2$  km) at a distance of  $110 \pm 20$  km inland from the coast. The shallow (<60 km depth) mantle velocity increases by 5% from WA to EA between E000 to E012, as controlled by the surface wave phase velocities [Lawrence *et al.*, 2006a]. The lowermost layer (half-space in this parameterization) increases by 5–7.5% from west to east (Figure 9). Between 20 and 80 km inland, a thick (5–15 km) low-velocity anomaly is observed at the surface. Inland from the TAM the crust thins again to ( $35 \pm 2$  km). There is little evidence of a low-velocity anomaly just beneath the East Antarctic Plateau except at E030.

[33] At first glance, the uncertainty in Moho depth ( $\sim 2$  km) may appear to indicate that the crustal “root” beneath the crest of the TAM is as thin as 1 km and as thick as 9 km. However, parameter tradeoff between seismic velocities above and depth to an interface cause much of this uncertainty. The uncertainties themselves are obtained by examining less optimal models, which possess particular biases in data misfit and model parameter tradeoff. By comparing only less optimal models between different stations with similar parameter biases (e.g., all models with higher mean crustal velocity than the most optimal model) indicates that the crustal root is  $5 \pm 2$  km.

[34] Along the N-S subarray (Figure 10), the profile is remarkably uniform with crustal thickness averaging 35 km. Excluding the coastal stations at the north end of the subarray, the maximum deviation is 4 km and the average deviation is less than 2 km. Thick, shallow low-velocity layers are present beneath stations in the Wilkes Subglacial Basin (N036–N060) and the Aurora Subglacial Basin (N092 and N100). The average upper mantle

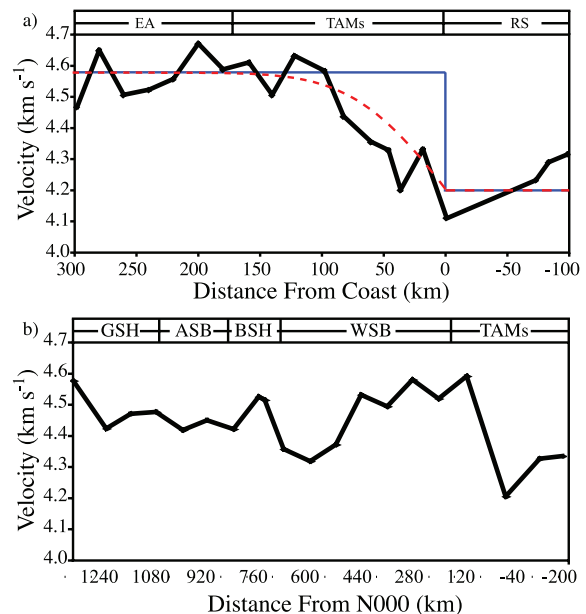


**Figure 9.** Seismic velocity at 100 km depth varies with (a) distance from the coast along the E-W profile and (b) distance from N000 along the N-S profile. Geographic features are labeled as East Antarctica (EA), Transantarctic Mountains (TAM), Ross Sea (RS), Gamburtsev Subglacial Highlands (GSH), Aurora Subglacial Basin (ASB), Belgica Subglacial Highlands (BSH), and Wilkes Subglacial Basin (WSB). The mantle velocities are higher beneath EA than the RS, with the transition occurring beneath the TAM. The red dashed line in Figure 9a represents a half-space heating model for horizontal conduction of heat from the Ross Sea to the TAM, with  $\kappa = 10^{-6} \text{ m s}^{-1}$ , a temperature contrast between EA and RS of  $\Delta T = 250^\circ\text{C}$ ,  $dV_s/dT = 1.2 \text{ km s}^{-1} \text{ C}^{-1}$ , and a time since onset of heating of 65 Ma. The solid blue line represents the starting model at 65 Ma.

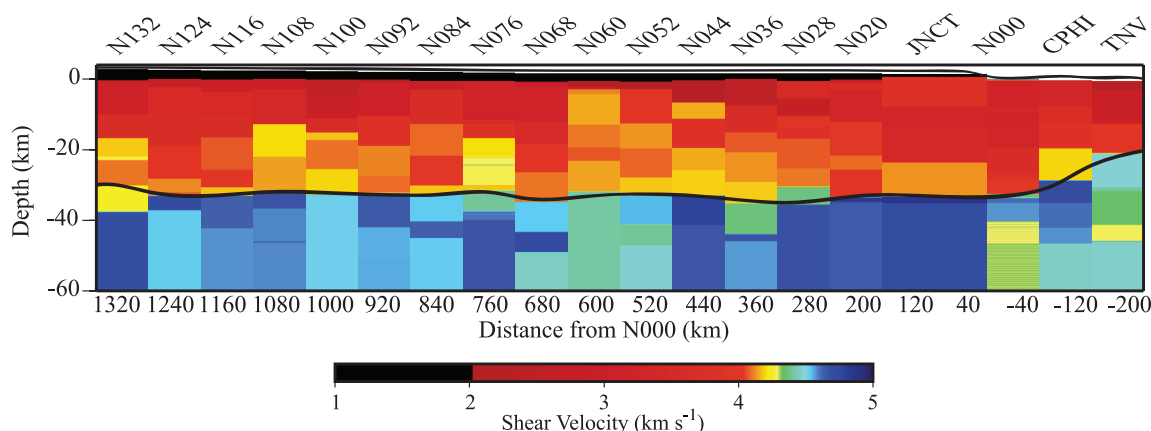


**Figure 10.** Two-dimensional profile of shear velocity for the N-S subarray across the TAM into the East Antarctic interior. The location of the profile is shown in Figure 6a.

seismic velocity is  $4.5 \pm 0.1 \text{ km s}^{-1}$  (Figure 9). The highest upper mantle seismic velocities occur on the inland side of the TAM and into the northeastern portion of the Wilkes Subglacial Basin (JNCT–N044), the Belgica Subglacial Highlands (N078), and Vostok Subglacial Highlands (N132). The lowest upper mantle seismic velocities occur beneath the coastal front (N000) and within the southern portion of the Wilkes Subglacial Basin (N052 and N060). Either the large station spacing (80–120 km) of the N-S subarray near the TAM may be too large to observe a crustal root, or the crustal root is not present farther north.

## 5.2. Forward Modeling: Free-Air Gravity and Topography

### 5.2.1. Data Set and Methodology

[35] The maps of crustal thickness and constraints on mantle density variations obtained from TAM-SEIS allow us to evaluate regional gravity and compensation models in more detail than previous studies. We compare 2-D profiles of observed free-air gravity with theoretical free-air gravity calculated from 2-D density models and observed surface and bedrock topography.

[36] The US National Science Foundation’s Support Office for Aerogeophysical Research (SOAR) surveyed gravity, magnetic intensity, and surface and bedrock topography around the E-W trending subarray in the 1999/2000 austral summer [Studinger *et al.*, 2004]. An airborne geophysical survey was likewise flown by SOAR along the N-S subarray in 2001/2002 [Blankenship *et al.*, 2001; Holt, 2001; Richter *et al.*, 2001]. Additional

gravity and topography data in the Ross Sea are made available through the Antarctic Digital Gravity Synthesis (ADGRAV, <http://www.marine-geo.org/antarctic/gravity/>, 2004) and BEDMAP [Lythe *et al.*, 2001]. The locations of the surveys are shown in Figure 1 overlain on a map of compiled regional free-air gravity measurements. We impose the following model constraints: mean topography, bathymetry, and ice thickness. A 20 km radius moving average is applied to each datum along the 2-D profiles in order to dampen the shorter (<20 km) wavelength topography, ice thickness, and free-air gravity anomalies. The standard deviation of the measured free-air gravity within each 20 km radius provides a good measure of the short-wavelength heterogeneity. These shorter wavelength anomalies are of less interest for regional tectonic studies. Ice density ( $920 \text{ kg m}^{-3}$ ), water density ( $1003 \text{ kg m}^{-3}$ ), sediment density ( $2400 \text{ kg m}^{-3}$ ), crustal density ( $2800 \text{ kg m}^{-3}$ ), and mantle density ( $3300 \text{ kg m}^{-3}$ ), are considered constant for the starting models.

[37] The gravity anomalies,  $g_z(x, z)$ , are calculated by integrating the 2-D Green’s function for gravitational potential,

$$g_z(x, z) = -2G \int_{S_0} \Delta\rho(x_0, z_0) \cdot \frac{(z - z_0)}{(x - x_0)^2 + (z - z_0)^2} dx_0 dz_0, \quad (2)$$

where  $G$  is the gravitational constant,  $x_0$  and  $z_0$  are the locations along the profile in the vertical plane  $S_0$ , and  $\Delta\rho(x_0, z_0)$  is the location dependent density anomaly [e.g., Turcotte and Schubert, 1982]. The integration is computed with discrete areas 0.05 km thick by 1 km wide. This discretization is

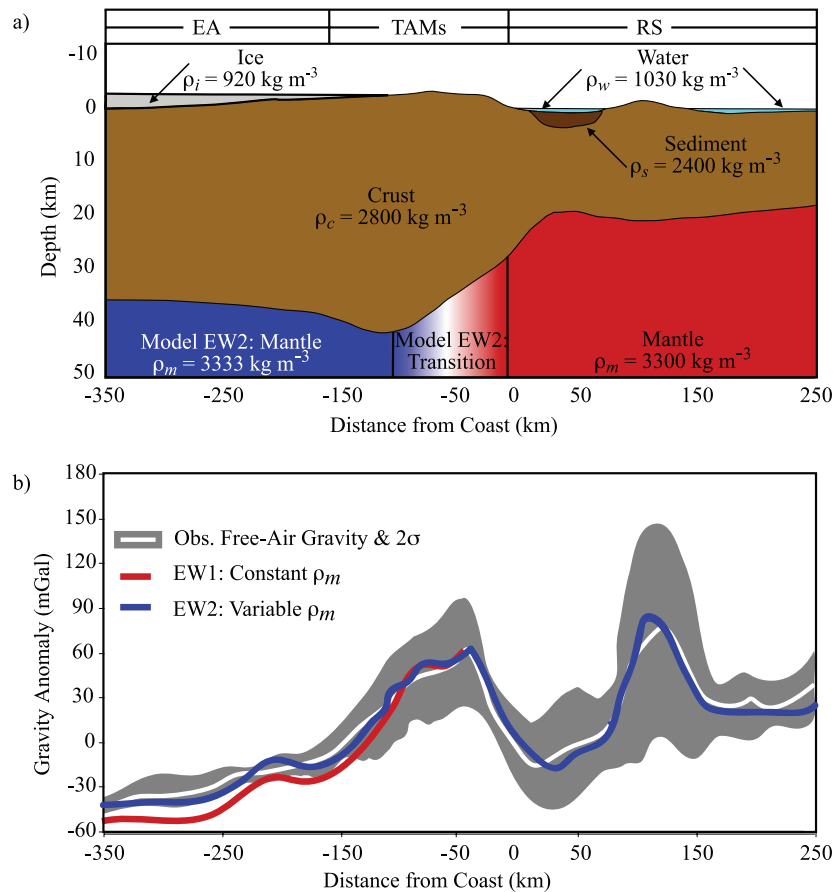


**Figure 11.** (a) Two-dimensional density models. (b) Theoretical free-air gravity with observed free-air gravity (white line). In model EW1, the bathymetry, topography, bedrock elevations are constrained by geophysical observations [Lythe *et al.*, 2001; Blankenship *et al.*, 2001], while the Moho topography from this study is augmented with results from Bannister *et al.* [2003], Cooper *et al.* [1997], and Trehu [1989]. In model EW2 (blue), the interface topography is the same, but mantle density increases by 1% from the Ross Sea (RS) to East Antarctica (EA) beneath the Transantarctic Mountains (TAM). The theoretical gravity of density model EW2 (blue) provides a somewhat better fit to the observed free-air gravity than model EW1 (red).

sufficiently small to model 20 km smoothed free-air gravity and Moho depths that are interpolated from 20 km to 80 km spacing. The models are extrapolated 200 km beyond the dimension of each gravity profile to minimize edge effects.

### 5.2.2. Predicted Gravity Anomalies Due to Crustal Thickness

[38] We created a 2-D density model, EW1, with smoothed Moho topography from our seismic models as a density interface. Model EW1 provides an excellent match between calculated and observed free-air gravity anomalies across the Transantarctic Mountains and into the Ross Sea (Figure 11). Beneath the Ross Sea, where broadband seismic data is lacking, we extrapolate the Moho topography on the basis of previous work

[Bannister *et al.*, 2003; Cooper *et al.*, 1997; Trehu, 1989]. A thick sedimentary (>3 km) basin is modeled between the coast and Ross Island on the basis of active seismic studies [Cooper *et al.*, 1987; Hamilton *et al.*, 2001] and the Cape Roberts Drilling Project [Cape Roberts Science Team, 2000]. The modeled gravity anomalies fit within one standard deviation of the observed gravity anomalies for the Ross Sea and Transantarctic Mountains. Inland from the Transantarctic Mountains model EW1 underestimates the gravity such that the misfit is greater than two standard deviations from the mean observed gravity.

### 5.2.3. Thermal Evolution of the TAM

[39] Extension in the West Antarctic Rift System (WARS) from the Cretaceous onward [Behrendt,



1999; *Behrendt et al.*, 1991a, 1991b] must have raised upper mantle temperatures in the WARS and may have perturbed the adjacent TAM lithosphere. *ten Brink and Stern* [1992] proposed that much of the uplift of the TAM occurred as a result of thermal buoyancy from horizontal heat conduction from warmer Ross Sea upper mantle. The TAMSEIS seismic observations are generally consistent with this model. Surface wave [Lawrence *et al.*, 2006a] and body wave tomography [Watson *et al.*, 2006] observed low velocities beneath the Ross Sea, moderate velocities beneath the TAM, and high velocities beneath EA. In addition, Lawrence *et al.* [2006b] observed a transition from high upper mantle attenuation in the Ross Sea to lower attenuation in EA that occurs between the coast and 140 km inland, and attributed this to upper mantle temperature variations. Here we observe seismic velocity variation from  $\sim 4.55$  km s<sup>-1</sup> in EA to  $\sim 4.2$  km s<sup>-1</sup> in WA at 100 km depth (Figure 9). The coincidence of low velocity and high attenuation in the Ross Sea indicates increased temperature. The temperature derivatives of velocity and quality factor [Karato, 1993; Faul and Jackson, 2005] indicate that the Ross Sea upper mantle is 200–300 K warmer than East Antarctic mantle [Lawrence *et al.*, 2006a, 2006b; Watson *et al.*, 2006].

[40] We model the shear velocity variation at 100 km depth in our results (Figure 9a) with a half-space heating/cooling model for horizontal heat conduction of  $\Delta T(x) = \Delta T_{RS-EA}(x/2\sqrt{\kappa t})$  [e.g., Turcotte and Schubert, 1982], where the velocity-temperature derivative ( $dV_S/dT$ ) is  $1.2 \times 10^{-3}$  km s<sup>-1</sup> as appropriate for 100 km depth and a mantle temperature of 1350°C [Faul and Jackson, 2005],  $x$  is the distance from edge of the EA plate (corresponding to the TAM coast),  $\kappa$  is the thermal diffusivity ( $10^{-6}$  m<sup>2</sup> s<sup>-1</sup>), and  $t$  is the time since the onset of conductive heating. A grid search provides the best-fit solution (red dashed line in Figure 9a) to the observed seismic velocities with a  $\Delta T = 275 \pm 35^\circ\text{C}$  between EA and RS and a time of  $t = 65 \pm 10$  Ma (blue solid line Figure 9a). The error bounds are determined using a bootstrap method. For modeling purposes we assume that the RS mantle is maintained at elevated temperatures as a result of small-scale convection associated with rifting, volcanism, and broad extension in the WARS. The results are nonunique because of the velocity-temperature derivative and thermal diffusivity may change as a result of composition, volatile content, depth, and temperature itself. However, the good agreement between modeled and observed

velocity lends credence to the hypothesis that the mantle beneath the TAM warmed over the past  $\sim 65$  Ma as a result of conductive heating from WA. The timing and temperature variation estimates found here are also in good agreement with the  $\sim 70$  Ma estimates of *ten Brink and Stern* [1992], which are inferred from surface heat flow measurements and the geological history.

#### 5.2.4. Effects of Mantle Density and Sediment Load

[41] The substantial increase in mantle temperatures (200–300°C) from  $\sim 150$  km inland to the coast for a depth range of  $\sim 80$  to  $\sim 250$  km is likely accompanied by a significant density variation. With a reasonable thermal coefficient of expansion ( $\alpha_{th} = 3.5 \times 10^{-5}$  K<sup>-1</sup>) we estimate that East Antarctic mantle is  $\sim 1\%$  denser than the Ross Sea mantle. Imposing this 1% mantle density increase under East Antarctica to a depth of 200 km significantly improves the fit to gravity anomalies beneath East Antarctica (model EW2).

[42] Sediment layers have less effect on the gravity signal than Moho and surface topography due to the larger topography of the Moho and the larger density contrast of the surface. The gravity misfit within the Victoria Land Basin decreases due to the addition of a thick ( $\sim 4$  km) sedimentary basin to both EW1 and EW2. However, sedimentary layers near the Wilkes Subglacial Basin increase the gravity misfit for model EW1 and require larger ( $>1\%$ ) mantle density anomalies to maintain low misfit for model EW2. *Studiver et al.* [2004] also found little evidence in favor of a thick ( $>1$  km) low-density sedimentary basin between 150 and 350 km from the coast. For the E-W profile we model no sediment beneath the ice.

[43] Both density models along the E-W line (EW1 and EW2) yield a large mass/load deficit inland of the Transantarctic Mountains, and mass/load surplus underlying the Transantarctic Mountains and Mt. Erebus. Although previous studies have suggested that the TAM topographic load is compensated by a thick crustal root [Studiver *et al.*, 2004], the crustal root determined in this study (approximately 5 km of topography relative to EA) provides only partial compensation for observed TAM elevations. If model EW1 were allowed to isostatically equilibrate without flexural or dynamic support, EA would uplift while the Ross Sea would subside by  $\sim 2$  km. The  $\sim 9$  km of vertical fault offset observed at the coast [Hamilton *et al.*, 2001] suggests that the lithosphere is broken

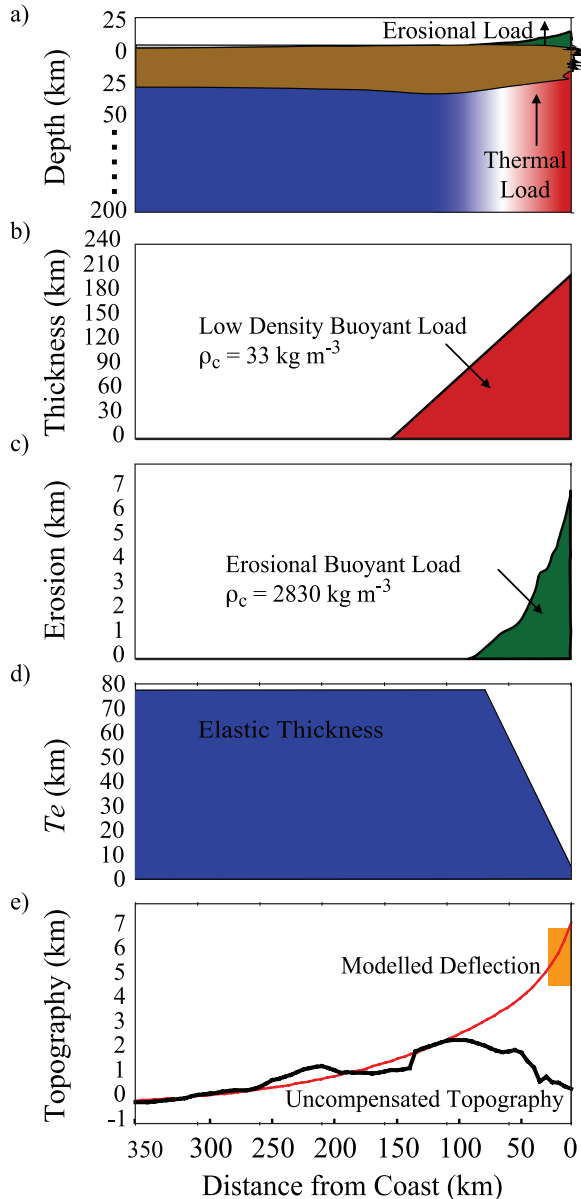


**Figure 12.** (a) A graphical depiction of the elastic flexural model used to describe the asymmetric uplift through the TAM after *ten Brink et al.* [1997]. The model uses buoyant loads from (b) thermal expansion and (c) erosion. (d) A variable elastic thickness is required to explain the large rock uplift and distant flexural bulge. (e) The model is designed to fit theoretical topography (red) to observed topography (black) that is not isostatically compensated and to match the predicted erosion (orange box).

and that flexure cannot support the current long-wavelength topography between EA and the WARS. Therefore, without a buoyant bottom load (mantle density anomaly), model EW1 fails to explain the current topography. The mantle density

anomaly of model EW2 balances the mass/loads between EA and the RS as a whole. Model EW2 requires only shorter-wavelength features, such as Mt. Erebus and the TAM, to be supported through nonisostatic compensation. Consequently, model EW2 is our preferred model.

### 5.2.5. Flexural Response

[44] We model the East Antarctic nonisostatic elevation residual as a flexural response [after *ten Brink et al.*, 1997] due to a buoyant line load,  $P$ , at the coast ( $x = 0 \text{ km}$ ), where the lithosphere may be broken. We only model the nonisostatic residual under the assumption that preexisting Moho and surface topography were compensated prior to uplift. Here, we briefly summarize the possible loading mechanisms that may have contributed to the Transantarctic Mountain uplift. *ten Brink et al.* [1997] offer a more detailed discussion of these positive and negative loads. Apatite fission track thermochronology [Fitzgerald, 1995] indicates that  $\sim 6 \text{ km}$  of exhumation, or buoyant erosional load, could have significantly contributed to the total buoyant load (Figure 12a). In order for erosional unloading to contribute at the onset of uplift, the predenudation elevation must have been at least  $500 \text{ m}$  [ten Brink and Stern, 1992] above the adjacent basin. After the initiation of uplift, increased topography encourages denudation regardless of preexisting topography. *ten Brink et al.* [1997] modeled a buoyant thermal load due to conductive heat transport from the young, thin (70 Ma, 125 km) lithosphere of West Antarctica to the old and thick (530 Ma, 250 km) lithosphere of East Antarctica. Consequent thermal expansion may result in a  $\sim 1\%$  density decrease at the front of the TAM, causing a thermally buoyant load. Our seismic and gravity models are consistent with a  $\sim 1\%$  density increase starting 50–100 km inland rather than at the coast, which provides further evidence for a buoyant load.

[45] The flexural model of the TAM is constrained by several observations. First, the fission track dating indicates  $\sim 6 \text{ km}$  uplift at the coast [Fitzgerald, 1995]. Elevations of sedimentary layers require uplift to decrease rapidly with distance from the coast, but extend several hundred kilometers inland [ten Brink et al., 1997]. The negative topographic flexural trough associated with the buoyant line load is assumed to be the negative bedrock topography of the Wilkes Basin, which is centered  $\sim 600 \text{ km}$  from the coast. At Cape Roberts, between 6 and 9 km of vertical separation are observed on N-S striking faults



**Table 3.** Parameters for Flexural Model

Parameter	Value	Equation	Units	Description
$w(x)$	-	$w_0 e^{-x/\alpha} \cos(x/\alpha)$	M	deflection
$w_0$	$7 \pm 1 \times 10^3$	$P\alpha^3/(4D)$	M	maximum uplift/deflection
$D$	$6.5 \times 10^{23}$	$E T_e^3/12(1 - \sigma^2)$	$\text{kg m}^2 \text{s}^{-2}$	flexural rigidity
$\alpha^4$	$4.4 \times 10^{20}$	$4D/(g\Delta\rho)$	$\text{m}^4$	flexural parameter
$T_e$	$5-100 \times 10^3$	-	M	elastic thickness
$E$	$8 \times 10^{10}$	-	$\text{kg m}^{-1} \text{s}^{-2}$	Young's modulus
$\sigma$	0.25	$\sigma$	0.25	Poisson's ratio
$q(x)$	-	$\Sigma(\rho\Delta h)$	$\text{kg m}^{-1} \text{s}^{-2}$	isostatic load
$G$	9.8	-	$\text{m s}^{-2}$	gravity
$\Delta\rho$	600	$(\rho_m - \rho_c)$	$\text{kg m}^{-3}$	Moho density contrast

[Hamilton *et al.*, 2001], indicating a relatively free boundary. Higher temperature, anelasticity [Lawrence *et al.*, 2006b], and faulting at the front of the TAM is consistent with a less rigid elastic plate. Farther inland the large distance to the compensating trough and lack of an anelastic layer beneath the lithosphere [Lawrence *et al.*, 2006b] indicate a more rigid plate. To account for the lateral variation in flexural rigidity, we employ a finite difference method to forward model the deflection, which allows laterally varying elastic thickness,  $T_e$  [Bodine *et al.*, 1981]. We forward model the deflection to minimize the misfit with nonisostatic residual topography, as well as the misfit between input and output buoyant erosional loads. Parameters of the forward modeling process are outlined in Table 3. A maximum upward deflection at the coast ( $w_0$ ) of  $6.0 \pm 1.0$  km and an elastic thickness ( $T_e$ ) of  $70 \pm 15$  km yields the appropriate nonisostatic relief at the appropriate distances (Figure 12e). This flexural model fits both EW1 and EW2 nonisostatic elevations. However, it is unreasonable that model EW1 requires flexural support across a fault system with 6 to 9 km of offset between East and West Antarctica [Hamilton *et al.*, 2001], so we prefer model EW2.

[46] Model EW2 provides an excellent fit to both the current free-air gravity anomaly and the flexural model. If the flexural model is correct, then the predeflected/eroded East Antarctic crust is  $35.5 \pm 1$  km thick at the coast and beyond 160 km from the coast. A thick ( $40 \pm 2$  km) predeflected/eroded crust between 100 and 120 km inland from the coast likely existed prior to the current formation of the TAM. A minimum denudation of 6 km at the coast and a gradual transition to 1% denser mantle starting  $100 \pm 50$  km inland are required to explain the flexural model. The gradual transition from high flexural rigidity and high mantle density

under the East Antarctica are likely due to conductive heating between East and West Antarctica [ten Brink *et al.*, 1997].

### 5.2.6. Compensation Mechanisms Along the N-S Line

[47] Along the N-S survey we model the free-air gravity with four models (Figure 13) to demonstrate the various compensation mechanisms and their relative fit to gravity. The gravity model NS1 demonstrates that surface topography, ice topography, and seismic Moho topography (from Figure 10) can account for the majority of the observed gravity anomaly. In model NS2 we include thick sedimentary basins at the southern end of the Wilkes Subglacial Basin (WSB) and Aurora Subglacial Basin (ASB) where low-velocity layers were observed in the upper crust in the receiver function analysis. These sedimentary layers significantly improve the fit to observed gravity within the WSB and ASB. Alternatively, shallow upper mantle density anomalies beneath the WSB (inferred from velocity and attenuation) could also contribute to the observed gravity anomalies. However, the shorter wavelength of these gravity anomalies ( $\sim 20$  km) is difficult to model with deeper mantle density anomalies. Nonuniqueness in the gravity modeling prevents identification of sediment basin shape and depth, but some form of sedimentary layering is required, and is also indicated by the receiver function data. Model NS3 applies the deflection from our flexural model to a 35 km thick crust with an excellent fit to the gravity, and little deviation from our seismic model. On the other hand, pure Airy compensation (model NS4) yields a poor fit to the observed gravity. A more accurate model is most likely represented by some combination of models NS2 and NS3.

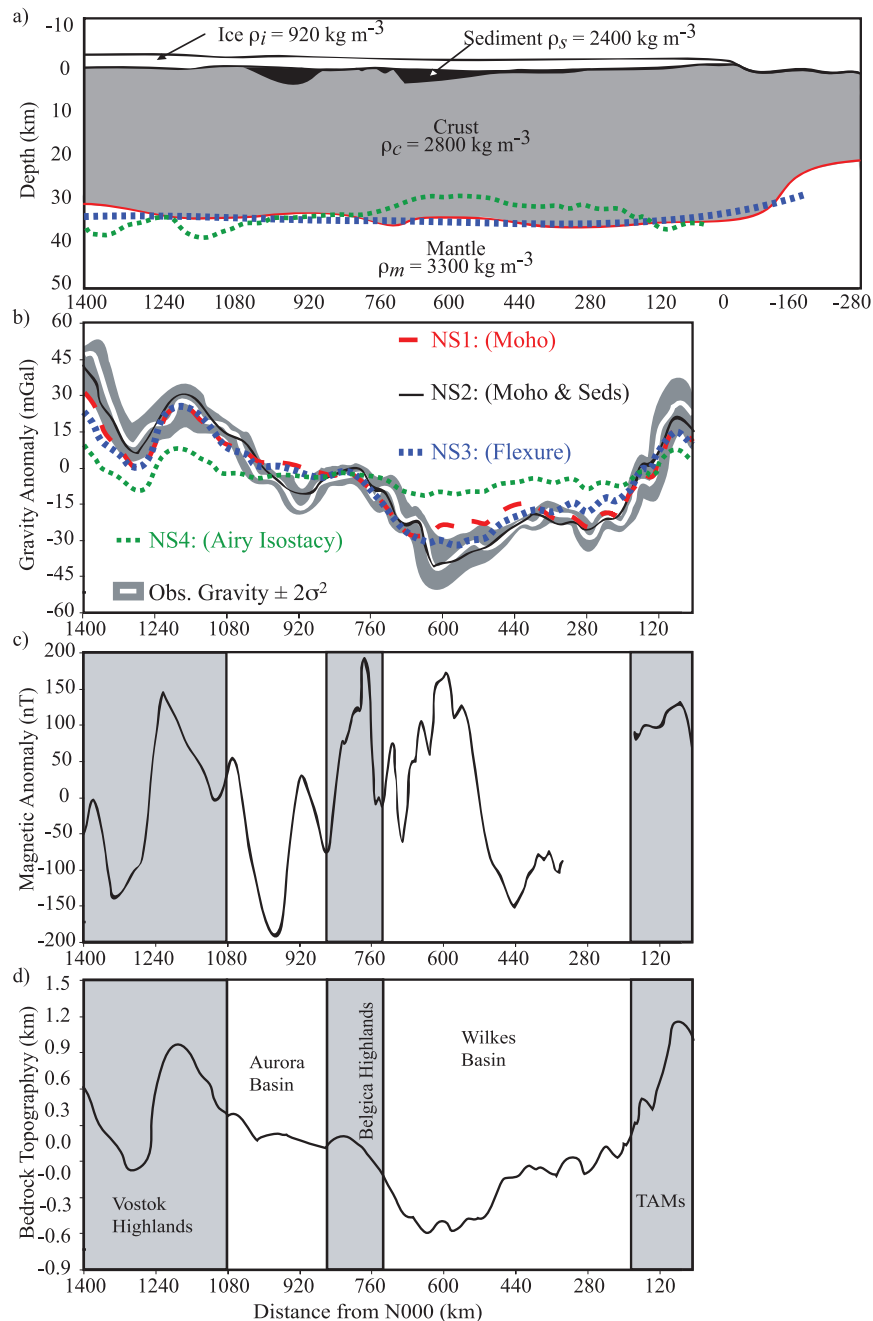
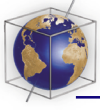


**Figure 13.** (a) A graphical representation of the density models. (b) Theoretical free-air gravity with 20-km smoothed observed free-air gravity. We employ four models with surface and bedrock topography from *Blankenship et al.* [2001]. Model NS1 includes only the Moho topography from Figure 8. NS2 also adds the sediment layers in place of low-velocity layers seen in Figure 8. NS3 uses the flexural model from Figure 12d for Moho topography. Model NS4 uses a Moho calculated to fit Airy isostatic equilibrium. (c) The magnetic anomalies demonstrate some correlation with (d) regional topographic features.

[48] The positive correlation between long-wavelength gravity and topography indicates flexural support or dynamic compensation over lateral distances greater than 1000 km [Turcotte and Schubert, 1982]. The upper mantle velocity

anomalies in the interior of East Antarctica are not variable enough to account for large temperature and density anomalies capable of such support. At the extent of our resolution ( $\sim 2$  km), the Aurora and Wilkes Subglacial Basins hint at thinner crust,



and suggest a very minor component of Airy compensation. However, the minor crustal thickness variations are insufficient to produce the large observed topography and the Airy compensation model produces a poor match to both the observed Moho topography and free-air gravity. The small difference between our seismic model NS2 (with a sedimentary basins) and the flexural model, NS3, indicates that flexural support is a likely candidate though some component of lateral mantle density variations (Pratt isostasy) cannot be ruled out. A strong lithosphere (modeled with a large elastic thickness,  $T_e = 75 \pm 15$  km) is capable of supporting the observed topography despite the observed gravity without significant Moho topography. This is consistent with observations of *Lawrence et al.* [2006b], which show that EA lacks an anelastic asthenosphere, and has thick lithospheric structure to a depth of 220 km or more.

[49] Seismic and gravity modeling indicate that thick (>1 km) layers of sediment may have deposited in the extreme southwestern edge of the Wilkes Subglacial Basin and in the Aurora Subglacial Basin. The application of this sediment as a load is difficult to model because of the question of timing and the tradeoff with a possible buoyant mantle load. Because the low-density sediments are surrounded by higher density crust, they may be described as a negative (or buoyant) load. However, if the sediment deposition postdates the flexure, the sediments may be considered a positive load applied to a flexurally compensated lithosphere. If the sedimentary basins are recent, they may be eroded from the Transantarctic Mountains, the Belgica Subglacial Highlands, and Vostok Subglacial Highlands. Otherwise they may represent erosion from prior elevated regions. The depth resolution of the Moho (~2 km) beneath the sedimentary basins is insufficient to determine if isostatic compensation was obtained prior to regional flexural support.

## 6. Discussion and Conclusions

[50] The E-W subarray imaged a small, but robust  $5 \pm 2$  km thick crustal “root” beneath the crest of the TAM. While the N-S subarray does not show a crustal root, this may be because the station spacing is too large. The ~40-km wide root that is observed beneath the E-W subarray may lie within the 80 to 120 km wide gaps between stations in the N-S subarray. The short-period phase velocity maps of *Lawrence et al.* [2006a] do not indicate a significant crustal difference between the north-

ern section and the region near the E-W array. However, the presence a small crustal root (~3 km) may not be resolvable using short-period phase velocities.

[51] The strong correlation between observed topographic and free-air gravity anomalies indicates that the Transantarctic Mountains are at least partially supported regionally by flexure, as the small size (~5 km) of the observed crustal root is insufficient to account for the elevation and gravity signatures of the TAM. Additionally, it is difficult to reconcile the extremely flat Moho of EA (less than 4 km vertical relief over 1000 km distance) with the large bedrock topography (>1 km) and ice thickness variation (>3 km) without dynamic or flexural support. Density and flexural models, constrained by seismic observations, demonstrate that the observed topography and uplift of the TAM may be explained by a combination of preexisting structure and flexural response due to buoyant erosional and thermal loads applied at the coast. The combination of the assumed buoyant erosional top load and the calculated thermally buoyant mantle bottom load are sufficient to uplift the TAM.

[52] While the flexural modeling assumes that the system was in isostatic compensation prior to uplift, it does not require a flat Moho or surface topography prior to uplift. In fact, reconstruction from the presumed current flexed state to the preflexure state indicates a preexisting ~5 km thick mountain root at ~110 km inland prior to TAM uplift. Such a preexisting root could have resulted from subduction related mountain building during the Ross Orogeny ~500 Ma, a remnant of subducted crust, or underplating. As a result, our seismic model agrees with the assertion from *Studiver et al.* [2004] that end-member models (pure flexure and pure Airy isostasy) cannot explain the data. Depending on the density and thickness of the observed root, the maximum topographic expression of the root’s buoyant load would be  $0.7 \pm .50$  km assuming a purely isostatic model. Flexural or dynamic compensation could easily reduce the topographic expression of the root by a factor of 2 or more. Consequently, a thin preexisting root (3–5 km) may not contradict evidence that the Beacon Supergroup sediments deposited on a relatively flat and level surface from the Devonian to the Mesozoic [*Barrett et al.*, 1986], whereas a thick root (>5 km) might.

[53] The exact causal relationship between the extension of West Antarctica and uplift through



the Transantarctic Mountains is difficult to constrain. While the adjacent uplift of the TAM and downward warping of the Victoria Land Basin suggest a Vening Meinesz rift model [Heiskanen and Vening Meinesz, 1958], the main uplift of the TAM may predate the formation of the Victoria Land Basin by as much as 20 Ma [Cape Roberts Science Team, 2000]. Additionally, to the south, the SERIS seismic experiment found no evidence for a down-warped sedimentary basin adjacent to the TAM, which demonstrates that the relationship between the TAM and the WARS is not constant along the mountain front [Stern and ten Brink, 1989]. West Antarctica is not uniform in structure or degree of extension along the length of the TAM [Bentley, 1991]. Therefore we are encouraged by the fact that the flexural model does not require the absence or presence of an adjacent extension or subsidence within the WARS.

[54] The seismic, gravity, and flexure models simply require that a buoyant thermal load exists beneath the TAM. Extension within the WARS is not necessary to explain the uplift. Simple conductive heating along the edge of the older, colder East Antarctic mantle by proximity to the younger, warmer West Antarctica can cause the uplift. The relatively modest seismic velocity perturbations within any one region suggest that the uplift of the TAM is not a result of one unique structure, but the combined structures of the WARS, TAM, and EA. The relatively uniform long-wavelength structures imaged by Danesi and Morelli [2001] and Ritzwoller et al. [2001] suggest that the buoyant thermal load observed in the Ross Sea region may also be found along the entire length of the mountain front. While the vertical cross-section along the coast (Figure 7c), the phase velocity maps of Lawrence et al. [2006a], and the body wave tomography of Watson et al. [2006] demonstrate that low velocities are largest near Ross Island, the variation along the front of the TAM is less than half of the variation across the TAM. The buoyant erosional load is clearly visible in the relief of bedrock topography along the front of the TAM [Lythe et al., 2001]. Consequently, it is possible that the TAM may have simply uplifted everywhere that the older, colder East Antarctic lithosphere came in contact with the younger, warmer lithosphere beneath West Antarctica. The low velocities in the shallow mantle concentrated near Ross Island may simply represent even lower mantle temperatures near the Ross Archipelago than elsewhere along the mountain front.

[55] The seismic and geophysical analyses conducted here agree with the hypothesis that East Antarctica has a thicker, colder, and denser crust and lithosphere than the adjacent West Antarctic Rift System. Joint receiver function and phase velocity analysis demonstrates that EA crust is 15 km thicker than RS crust. The crust reaches its maximum thickness ( $\sim 40$  km) beneath the crest of the mountains ( $\sim 100$  km from the coast) where the upper mantle transitions from cold and dense to warm and buoyant. The mantle temperature and density difference between EA and the RS likely aided in the asymmetric uplift of the TAM by providing a buoyant bottom load.

## Acknowledgments

[56] We thank Mitchell Barklage, Bruce Beaudoin, Maggie Benoit, Jerry Bowling, James Conder, Audrey Huerta, Bruce Long, Bob Osburn, Tim Parker, Sara Pozgay, Moira Pyle, Brian Shiro, Rigobert Tibi, Tim Watson, and many other individuals for assistance in preparing, deploying, and retrieving TAMSEIS stations and data. Portable seismic instrumentation for this project was obtained from the PASSCAL program of the Incorporated Research Institutions in Seismology (IRIS), and data handling assistance was provided by the IRIS Data Management System. We thank Tim Stern and Anya Reading for thorough and very helpful reviews, which greatly improved the quality of this manuscript. This research was conducted with support from NSF grants OPP9909603 and OPP9909648.

## References

- Ammon, C. J. (1991), The isolation of receiver effects from teleseismic P waveforms, *Bull. Seismol. Soc. Am.*, *81*(6), 2504–2510.
- Ammon, C. J., G. E. Randall, and G. Zandt (1990), On the nonuniqueness of receiver function inversions, *J. Geophys. Res.*, *95*(B10), 15,303–15,318.
- Bannister, S., R. K. Snieder, and M. L. Passier (2000), Shear-wave velocities under the Transantarctic Mountains and Terror Rift from surface wave inversion, *Geophys. Res. Lett.*, *27*, 281–284.
- Bannister, S., J. Yu, B. Leitner, and B. L. N. Kennett (2003), Variations in crustal structure across the transition from West to East Antarctica, Southern Victoria Land, *Geophys. J. Int.*, *155*(3), 870–880.
- Barrett, P. J., D. H. Elliot, and J. F. Lindsey (1986), The Beacon Supergroup (Devonian-Triassic) and Ferrar Group (Jurassic) in the Beardmore Glacier area, Antarctica, in *Geology of the Central Transantarctic Mountains, Antarct. Res. Ser.*, vol. 36, edited by M. D. Turner and J. F. Spletstocser, pp. 339–428, AGU, Washington, D. C.
- Behrendt, J. C. (1999), Crustal and lithospheric structure of the West Antarctic Rift System from geophysical investigations — A review, *Global Planet. Change*, *23*, 25–44.
- Behrendt, J. C., H. J. Duerbaum, D. Damaske, R. Saltus, W. Bosum, and A. K. Cooper (1991a), Extensive volcanism and related tectonism beneath the Ross Sea continental shelf,



- Antarctica: Interpretation of an aeromagnetic survey, in *Geological Evolution of Antarctica*, edited by J. W. Thomson, pp. 299–304, Cambridge Univ. Press, New York.
- Behrendt, J. C., W. E. LeMasurier, A. K. Cooper, F. Tessensohn, A. Trehu, and D. Damaske (1991b), Geophysical studies of the West Antarctic Rift System, *Tectonics*, *10*(6), 1257–1273.
- Bentley, C. R. (1991), Configuration and structure of the subglacial crust, in *The Geology of Antarctica*, edited by R. J. Tingey, pp. 335–364, Clarendon, Oxford, U. K.
- Berg, J. H., R. J. Moscati, and D. L. Herz (1989), A petrologic geotherm from a continental rift in Antarctica, *Earth Planet. Sci. Lett.*, *93*(1), 98–108.
- Blackman, D. K., R. P. Von Herzen, and L. A. Lawver (1987), Heat flow and tectonics in the western Ross Sea, Antarctica, in *The Antarctic Continental Margin: Geology and Geophysics of the Western Ross Sea*, edited by F. J. Davey, pp. 179–189, Circum-Pac. Council for Energy and Nat. Resour., Houston, Tex.
- Blankenship, D. D., D. L. Morse, C. A. Finn, R. E. Bell, M. E. Peters, S. D. Kempf, S. M. Hodge, M. Studinger, J. C. Behrendt, and J. M. Brozena (2001), Geologic controls on the initiation of rapid basal motion for West Antarctic ice streams: A geophysical perspective including new airborne radar sounding and laser altimetry results, in *The West Antarctic Ice Sheet: Behavior and Environment*, *Antarct. Res. Ser.*, vol. 77, edited by R. A. Bindschadler, pp. 105–121, AGU, Washington, D. C.
- Bodine, J. H., M. S. Steckler, and A. B. Watts (1981), Observations of flexure and the rheology of the oceanic lithosphere, *J. Geophys. Res.*, *86*, 3695–3707.
- Bott, M. H. P., and T. A. Stern (1992), Finite element analysis of Transantarctic Mountain uplift and coeval subsidence in the Ross Embayment, *Tectonophysics*, *201*(3–4), 341–356.
- Busetti, M., G. Spadini, F. M. Van der Wateren, S. Cloetingh, and C. Zanolla (1999), Kinematic modeling of the West Antarctic Rift System, Ross Sea, Antarctica, in *Global and Planetary Change*, edited by S. A. P. L. Cloetingh, pp. 79–103, Elsevier, New York.
- Cande, S. C., and R. B. Leslie (1986), Late Cenozoic tectonics of the Southern Chile Trench, *J. Geophys. Res.*, *91*, 451–496.
- Cande, S. C., J. M. Stock, R. D. Müller, and T. Ishihara (2000), Cenozoic motion between East and West Antarctica, *Nature*, *404*, 145–150.
- Cape Roberts Science Team (2000), Studies from the Cape Roberts Project, Ross Sea, Antarctica, Initial report on CRP-3, *Terra Antarct.*, *7*, 1–209.
- Chang, S.-J., C.-E. Baag, and C. A. Langston (2004), Joint analysis of teleseismic receiver functions and surface wave dispersion using the genetic algorithm, *Bull. Seismol. Soc. Am.*, *94*(2), 691–704.
- Chery, J., F. Lucazeau, M. Daignières, and J. P. Vilotte (1992), Large uplift of rift flanks: A genetic link with lithospheric rigidity?, *Earth Planet. Sci. Lett.*, *112*, 195–211.
- Clitheroe, G., O. Gudmundsson, and B. L. N. Kennett (2000), Sedimentary and upper crustal structure of Australia from receiver functions, *Aust. J. Earth Sci.*, *47*(2), 209–216.
- Cogley, J. G. (1984), Deglacial hypsometry of Antarctica, *Earth Planet. Sci. Lett.*, *67*, 151–177.
- Cooper, A. K., F. J. Davey, and J. C. Behrendt (1987), Seismic stratigraphy and structure of the Victoria Land Basin, Western Ross Sea, Antarctica, in *The Antarctic Continental Margin: Geology and Geophysics of the Western Ross Sea*, edited by F. J. Davey, pp. 27–76, Circum-Pac. Council for Energy and Nat. Resour., Houston, Tex.
- Cooper, A. K., H. Trey, G. Cochrane, F. Egloff, M. Busetti, and Acrup Working Group (1997), Crustal structure of the Southern Central Trough, Western Ross Sea, in *The Antarctic Region: Geological Evolution and Processes. Proceedings of the VIIth International Symposium on Antarctic Earth Sciences, Siena 1995*, edited by C. A. Ricci, pp. 637–642, Terra Antarct., Siena, Italy.
- Dalziel, I. W. D. (1992), Antarctica: A tale of two supercontinents, *Annu. Rev. Earth Planet. Sci.*, *20*, 501–526.
- Dalziel, I. W. E., and D. H. Elliot (1982), West Antarctic: Problem child of Gondwanaland, *Tectonics*, *1*, 3–19.
- Danesi, S., and A. Morelli (2001), Structure of the upper mantle under the Antarctic Plate from surface wave tomography, *Geophys. Res. Lett.*, *28*, 4395–4398.
- Drewry, D. J. (1976), Sedimentary basins of the East Antarctic Craton from geophysical evidence, *Tectonophysics*, *36*, 301–314.
- Faul, U. H., and I. Jackson (2005), The seismological signature of temperature and grain size variations in the upper mantle, *Earth Planet. Sci. Lett.*, *234*, 119–134.
- Ferraccioli, F., F. Coren, E. Bozzo, C. Zanolla, S. Gandol, I. E. Tabacco, and M. Frezzotti (2001), Rifted crust at the East Antarctic Craton margin: Gravity and magnetic interpretation along traverse across the Wilkes Subglacial Basin region, *Earth Planet. Sci. Lett.*, *192*, 407–421.
- Fitzgerald, P. G. (1992), The Transantarctic Mountains of southern Victoria Land: The application of apatite fission track analysis to a rift shoulder uplift, *Tectonics*, *11*(3), 634–662.
- Fitzgerald, P. G. (1995), Cretaceous and Cenozoic exhumation of the Transantarctic Mountains: Evidence from the Kukri Hills of southern Victoria Land compared to fission track data from gneiss at DSDP site 270, paper presented at Seventh International Symposium on Antarctic Earth Sciences, Terra Antarct., Siena, Italy.
- Fitzgerald, P. G. (2002), Tectonics and landscape evolution of the Antarctic plate since the breakup of Gondwana, with an emphasis on the West Antarctic Rift System and the Transantarctic Mountains, *Bull. R. Soc. N. Z.*, *35*, 453–469.
- Fitzgerald, P. G., M. Sandiford, P. J. Barrett, and J. W. Gleadow (1986), Asymmetric extension associated with uplift and subsidence in the Transantarctic Mountains and Ross Embayment, *Earth Planet. Sci. Lett.*, *81*(1), 67–78.
- Hamilton, R. J., B. P. Luyendyk, C. C. Sorlien, and L. R. Bartek (2001), Cenozoic tectonics of the Cape Roberts Rift Basin and Transantarctic Mountains front, southwest of Ross Sea, Antarctica, *Tectonics*, *20*(3), 325–342.
- Heiskanen, W. A., and F. A. Vening Meinesz (1958), *The Earth and Its Gravity Field*, 470 pp., McGraw-Hill, New York.
- Holt, J. W. (2001), Airborne surveys conducted by SOAR for geologic studies in Antarctica, *Eos Trans. AGU*, *82*(20), Spring Meet. Suppl., Abstract GP42A-07.
- Janowski, E. J., and D. J. Drewry (1981), The structure of West Antarctic from geophysical studies, *Nature*, *291*, 17–21.
- Julia, J., C. J. Ammon, R. B. Herrmann, and A. M. Correig (2000), Joint inversion of receiver function and surface wave dispersion observations, *Geophys. J. Int.*, *143*, 99–112.
- Kanao, M., T. Shibutani, H. Negishi, and H. Tono (2002), Crustal structure around the Antarctic margin by teleseismic receiver function analyses, in *Antarctica at the Close of a Millennium*, edited by J. A. Gamble, D. N. B. Skinner, and S. Henrys, pp. 485–491, R. Soc. of N. Z., Wellington.
- Karato, S. (1993), Importance of anelasticity in the interpretation of seismic tomography, *Geophys. Res. Lett.*, *20*, 1623–1626.



- Koper, K. D., M. E. Wyssession, and D. A. Wiens (1999), Multimodal function optimization with a niching genetic algorithm: A seismological example, *Bull. Seismol. Soc. Am.*, *89*(4), 978–988.
- Langston, C. A. (1979), Structure under Mount Rainier, Washington, inferred from teleseismic body waves, *J. Geophys. Res.*, *83*, 4749–4762.
- Lawrence, J. F., and D. A. Wiens (2004), Combine receiver-function and surface wave phase-velocity inversion using a niching genetic algorithm: Application to Patagonia, *Bull. Seismol. Soc. Am.*, *94*(3), 977–987.
- Lawrence, J. F., D. A. Wiens, A. A. Nyblade, S. Anandakrishnan, P. J. Shore, and D. Voigt (2006a), Rayleigh wave phase velocity analysis of the Ross Sea, Transantarctic Mountains, and East Antarctica from a temporary seismograph array, *J. Geophys. Res.*, *111*, B06302, doi:10.1029/2005JB003812.
- Lawrence, J. F., D. A. Wiens, A. A. Nyblade, S. Anandakrishnan, P. J. Shore, and D. Voigt (2006b), Upper mantle thermal variations beneath the Transantarctic Mountains inferred from teleseismic S-wave attenuation, *Geophys. Res. Lett.*, *33*, L03303, doi:10.1029/2005GL024516.
- LeMasurier, W. E., and J. W. Thomson (Eds.) (1990), *Volcanoes of the Antarctic Plate and Southern Oceans*, *Antarct. Res. Ser.*, vol. 48, AGU, Washington D. C.
- Ligorria, J. P., and C. J. Ammon (1999), Iterative deconvolution and receiver-function estimation, *Bull. Seismol. Soc. Am.*, *89*, 1395–1400.
- Lythe, M. B., D. G. Vaughan, and B. Consortium (2001), BEDMAP: A new ice thickness and subglacial topographic model of Antarctica, *J. Geophys. Res.*, *106*, 11,335–11,351.
- Mahfoud, S. W. (1995), Niching methods for genetic algorithms, Ph.D. thesis, Univ. of Ill., Champaign.
- Morelli, A., and S. Danesi (2004), Seismological imaging of the Antarctic continental lithosphere: A review, *Global Planet. Change*, *42*, 155–165.
- Park, J., and V. Levin (2000), Receiver functions from multiple-taper spectral correlation estimates, *Bull. Seismol. Soc. Am.*, *90*(6), 1507–1520.
- Randall, G. E. (1989), Efficient calculation of differential seismograms for lithospheric receiver functions, *Geophys. J. Int.*, *99*(3), 469–481.
- Reading, A., B. Kennett, and M. Sambridge (2003), Improved inversion for seismic structure using transformed, S-wave-vector receiver functions: Removing the effect of the free surface, *Geophys. Res. Lett.*, *30*(19), 1981, doi:10.1029/2003GL018090.
- Richter, T., J. W. Holt, and D. D. Blankenship (2001), Airborne gravity over East Antarctica, in *KIS 2001: Proceedings of the International Symposium on Kinematic Systems in Geodesy, Geomatics and Navigation*, pp. 576–585, Univ. of New Brunswick, Fredericton, Canada.
- Ritzwoller, M. H., N. M. Shapiro, A. L. Levshin, and G. M. Leahy (2001), Crustal and upper mantle structure beneath Antarctica and surrounding oceans, *J. Geophys. Res.*, *106*, 30,645–30,670.
- Sheehan, A. F., G. A. Abers, C. H. Jones, and A. L. Lerner-Lam (1995), Crustal thickness variations across the Colorado Rocky Mountains from teleseismic receiver functions, *J. Geophys. Res.*, *100*, 20,391–20,404.
- Sieminski, A., E. Debayle, and J. J. Leveque (2003), Seismic evidence for deep low-velocity anomalies in the transition zone beneath West Antarctica, *Earth Planet. Sci. Lett.*, *216*, 645–661.
- Smith, A. G., and D. J. Drewry (1984), Delayed phase change due to hot asthenosphere causes Transantarctic uplift?, *Nature*, *309*, 536–538.
- Stern, T. A., and U. S. ten Brink (1989), Flexural uplift of the Transantarctic Mountains, *J. Geophys. Res.*, *94*, 10,315–10,330.
- Studinger, M., G. D. Karner, R. E. Bell, V. Levin, C. A. Raymon, and A. A. Tikku (2003), Geophysical models for the tectonic framework of the Lake Vostok region, East Antarctica, *Earth Planet. Sci. Lett.*, *216*, 663–677.
- Studinger, M., R. E. Bell, W. R. Buck, G. D. Karner, and D. D. Blankenship (2004), Subglacial geology inland of the Transantarctic Mountains in light of new aerogeophysical data, *Earth Planet. Sci. Lett.*, *220*, 391–408.
- ten Brink, U. S., and T. A. Stern (1992), Rift flank uplifts and hinterland basins: Comparison of the Transantarctic Mountains with the great escarpment of southern Africa, *J. Geophys. Res.*, *97*, 569–585.
- ten Brink, U. S., S. Bannister, B. C. Beaudoin, and T. A. Stern (1993), Geophysical investigations of the tectonic boundary between East and West Antarctica, *Science*, *261*, 45–50.
- ten Brink, U. T., R. I. Hackney, S. Bannister, T. A. Stern, and Y. Makovsky (1997), Uplift of the Transantarctic Mountains and the bedrock beneath the East Antarctic ice sheet, *J. Geophys. Res.*, *102*, 27,603–27,621.
- Tingey, R. J. (1991), *The Geology of Antarctica*, Oxford Univ. Press, New York.
- Trehu, A. M. (1989), Crustal structure in the Ross Sea, Antarctica: Preliminary results from GANOVEX V, *Eos Trans. AGU*, *70*, 1344.
- Turcotte, D. L., and G. Schubert (1982), *Geodynamics: Applications of Continuum Physics to Geological Problems*, John Wiley, Hoboken, N. J.
- van der Beek, P., S. Cloetingh, and P. Andriessen (1994), Mechanisms of extensional basin formation and vertical motions at rift flanks: Constraints from tectonic modeling and fission track thermochronology, *Earth Planet. Sci. Lett.*, *121*, 417–433.
- Watson, T., A. Nyblade, D. A. Wiens, S. Anandakrishnan, M. Benoit, P. J. Shore, D. Voigt, and J. VanDecar (2006), P and S velocity structure of the upper mantle beneath the Transantarctic Mountains, East Antarctic craton, and Ross Sea from travel time tomography, *Geochem. Geophys. Geosyst.*, *7*, Q07005, doi:10.1029/2005GC001238.